Relevance of quadrupolar sound diffraction on flow-induced noise from porous-coated cylinders

Zamponi, R.; Avallone, F.; Ragni, D.; Schram, C.; van der Zwaag, S.

DOI
10.1016/j.jsv.2024.118430

Publication date
2024

Document Version
Final published version

Published in
Journal of Sound and Vibration

Journal of Sound and Vibration 583 (2024) 118430

Contents lists available at ScienceDirect

Journal of Sound and Vibration

journal homepage: www.elsevier.com/locate/jsvi

Relevance of quadrupolar sound diffraction on flow-induced noise from porous-coated cylinders

R. Zamponi [a,b,*], F. Avallone [c], D. Ragni [a], C. Schram [b], S. van der Zwaag [a]

[a] Delft University of Technology, Kluyverweg 1, Delft, 2629 HS, The Netherlands
[b] von Karman Institute for Fluid Dynamics, Waterloosesteenweg 72, Sint-Genesius-Rode, B-1640, Belgium
[c] Politecnico di Torino, Corso Duca degli Abruzzi 24, Torino, 10129, Italy

ARTICLE INFO

Keywords:
Aeroacoustics
Vortex shedding
Sound diffraction
Noise control
Coated cylinder
Porous materials

ABSTRACT

This paper elucidates the link between the near-wake development of a circular cylinder coated with a porous material in a low Mach-number flow and the related aerodynamic sound attenuation. It accomplishes this by formulating the cylinder flow-induced noise as a diffraction problem. The necessity for such an approach is driven by experimental evidence obtained through acoustic beamforming and particle-image-velocimetry measurements, which reveal that the dominant noise sources for a coated cylinder are not localised on the body surface but rather in the wake, specifically at the outbreak position of the shedding instability. The acoustic field at the vortex-shedding frequency can be hence modelled by considering a compact lateral quadrupole at this location and employing an exact Green's function tailored to a cylindrical geometry. Because of the diffraction of the sound waves radiated by the quadrupolar source on the cylinder surface, the resulting far-field directivity pattern resembles that of a dipole. The study demonstrates that the porous coating has the two-fold effect of decreasing the strength of the point quadrupole in the wake and moving its origin further downstream, reducing, in turn, the efficiency of the sound scattering. Consequently, the diffracted part of the acoustic field, which dominates the far-field noise for a bare cylinder in accordance with classical theory, provides a contribution that is comparable to the direct part. The results eventually indicate that quadrupolar sources must be considered to accurately predict the noise radiated from a porous-coated cylinder, even at low Mach numbers.

1. Introduction

The aerodynamic noise produced by a cylinder immersed in a transverse flow affects a large number of engineering applications, including landing-gear systems and high-speed trains. The tonal component of this noise source, commonly denoted as Aeolian tone, is associated with the shedding of vortical structures that periodically detach from opposite sides of the cylinder surface, forming the so-called von Kármán street [1]. In the classical view of the problem, the vortex shedding induces a fluctuating reaction force exerted by the body on the surrounding fluid that can be described by a distribution of surface dipoles following Curle's analogy [2]. At low Mach numbers and if the body is assumed to be acoustically compact, this surface term typically dominates over the volume term, which is produced by the unsteady velocity in the turbulent wake and can be modelled as a quadrupole [3]. However, the fluctuating reaction force should be interpreted only in terms of equivalent sound sources. As remarked by Powell [4], in practical applications, such force is exerted on a rigid surface and cannot generate acoustic energy. Hence, its origin must instead come from

* Corresponding author at: Delft University of Technology, Kluyverweg 1, Delft, 2629 HS, The Netherlands.
E-mail address: r.zamponi@tudelft.nl (R. Zamponi).

https://doi.org/10.1016/j.jsv.2024.118430
Received 3 January 2024; Received in revised form 30 March 2024; Accepted 5 April 2024
Available online 10 April 2024

the unsteady flow and is linked to the diffraction of the noise emissions from the quadrupolar sources by the body, which is an efficient sound-production mechanism for acoustically compact cases [4–7]. This vision does not conflict with the conventional view of the problem previously described and the experimental evidence that vortex shedding can be interpreted as a dipole source of sound [8]. As shown, for instance, by Gloerfelt et al. [9], it is possible to retrieve the dipolar nature of the noise generated by a circular cylinder in a transverse flow at low Mach numbers by modelling only the quadrupolar volume sources in the wake and using a tailored Green's function that accounts for the presence of the body, without directly considering the unsteady pressure at its surface. The conclusion that a quadrupole near a circular cylinder yields an induced dipole can also be deduced with the method of the image sources [10].

According to the theoretical framework outlined above, decreasing the unsteadiness of the von Kármán street has a beneficial effect on the emitted aerodynamic sound. Multiple efforts have thus been devoted to reducing the Aeolian tone by acting on the amplitude of the vortex shedding and the location where it begins [11]. One of the most promising passive flow-control strategies is to coat the surface of the cylinder with a porous material. Several experimental and numerical investigations have been carried out in the last decade to analyse the noise-mitigation performance achievable with a flow-permeable coating. A first study on the topic was performed by Sueki et al. [12], who demonstrated the effectiveness of this technological solution in reducing aerodynamic sound. Liu et al. [13] showed that, besides the noise attenuation, the integration of a metal-foam cover moves the vortex-shedding peak towards lower frequencies and narrows its bandwidth. This effect increases along with the thickness, porosity, and average pore dimension of the permeable layer. Interestingly, the far-field sound radiated by the coated cylinder was found to be dipolar in nature. Moreover, Geyer and Sarradj [14] tested several porous media and showed that materials that are highly permeable to air yield the best noise mitigation. In that case, a significant additional reduction was observed in the broadband range, particularly at higher Reynolds numbers. Similar findings were achieved by Geyer [15], who estimated the key parameters acting on the vortex-shedding tonal noise using the method of linear regression. He found that increasing the air-flow resistivity and thickness of the porous cover, as well as decreasing its porosity, results in a shift of the vortex-shedding Strouhal number towards higher values. Similarly, increasing the thickness and porosity and decreasing the air-flow resistivity leads to lower peak amplitudes of the Aeolian tone. Nonetheless, no definitive explanation for the physics behind these trends was provided, and no optimisation of the porous properties of the material was attempted. In this regard, Sharma et al. [16] demonstrated that a careful tuning of the air-flow permeability and the coating thickness with the varying Reynolds number is instrumental in achieving optimal noise mitigation.

From an aerodynamic perspective, numerous authors have investigated the near wake of a porous-coated cylinder to elucidate the related noise-reduction mechanisms. For instance, Sueki et al. [12] observed that porosity affects the flow past the body by further depriving momentum in the wake region, which is more uniform and delimited by thinner and more stable shear layers compared with that of the impermeable configuration having the same cylinder diameter. This phenomenon results in a mitigation of the unsteady motion of the shed vortices that, in turn, decreases the aerodynamic force fluctuations on the surface. Such a stabilisation effect of the oscillating wake was explained by Naito and Fukagata [17] in terms of slip velocity and fluid energy. Indeed, the presence of a non-zero velocity at the porous interface reduces the friction and weakens the detached eddies that destabilise the flow. In addition, the fluid that permeates the porous medium is subjected to a strong dissipation that consequently leads to low-energy flow ejected from the leeward part of the coated cylinder. Both effects contribute to forming more steady shear layers. Likewise, Showkat Ali et al. [18] highlighted that the most striking effect of the porous cover on the flow field is to shift the instability-development region downstream and decrease the turbulence kinetic energy. In this case, a drag increase was found due to the widening of the wake region and the lower velocities downstream of the body. Comparable findings were obtained for cylinders coated with metal foam by Aguiar et al. [19], who also observed a reduction in pressure drag due to the penetration of flow within the inner volume, and Xia et al. [20], who suggested that the larger vortex-formation length, identified by the location of the outbreak of the shedding, is caused by the weakened interactions between the shear layers at opposite sides of the body. Furthermore, Sadeghipour et al. [21] concluded that the distance from the cylinder at which the vortex shedding starts is directly linked to the permeability of the coating material.

All these studies confirm a link between the stabilisation of the wake-flow region and noise attenuation. According to the common view, suppressing the unsteady-vortex motion near the body leads to a lower aerodynamic force fluctuation exerted on its surface, which is responsible for the aeroacoustic sound [22]. Nevertheless, as discussed above, these noise sources must be intended as equivalent sources that result from a diffraction mechanism. In other words, they represent only one aspect of the acoustic problem and do not account for the actual production of acoustic energy. In this perspective, the definitive connection between the changes in the flow field and the sound mitigation due to the porous cover has yet to be clarified. The objective of the present paper is to elucidate this link by formulating the flow-induced noise of a coated cylinder as a diffraction problem [9]. The need for adopting a different approach than the conventional one based on Curle's analogy stems from the new experimental evidence provided in this research, which shows that the dominant sound sources, estimated with the acoustic-beamforming technique, are not detected on the surface of the porous body but in its wake, at the outbreak location of the vortex-shedding instability. An enhanced understanding of these noise-generation mechanisms would pave the way for designing optimised and more effective solutions to control the Aeolian tone, such as those recently proposed by Zamponi et al. [23], which support the theoretical framework developed in the present study.

The remainder of the document is structured as follows. A brief overview of the modelling of the Aeolian tone is given in Section 2. The measurement setup, already introduced by the authors in a recent work [24], is described in Section 3. In Section 4, the main results are outlined and discussed, highlighting the connection between the stabilisation of the wake-flow region and the noise attenuation provided by the porous coating with the support of analytical modelling. Finally, the conclusions are drawn in Section 5.

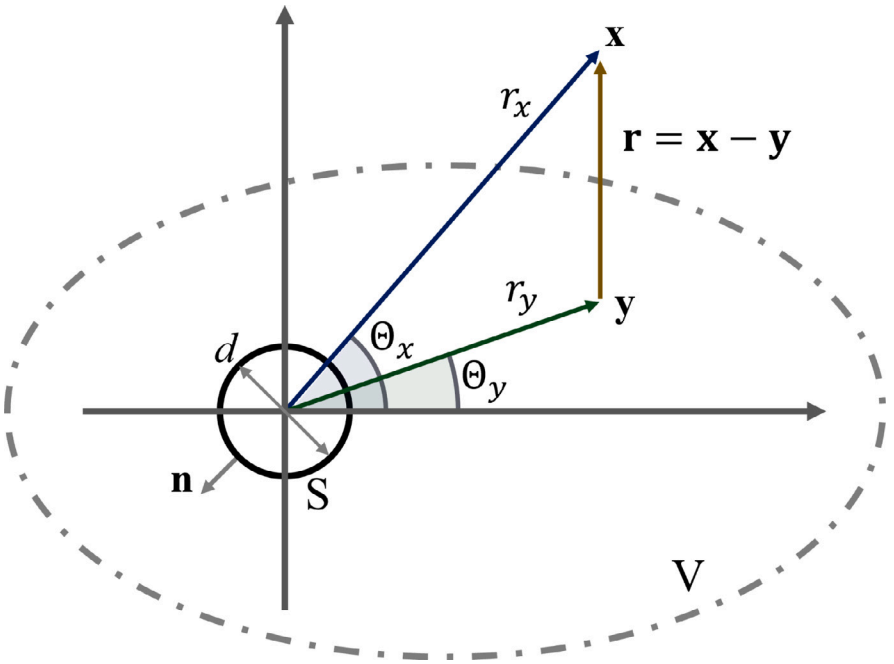

Fig. 1. Coordinate system defined for the formulation of the analytical model involving sound scattering by a cylinder with diameter d. *Source:* Picture adapted from Gloerfelt et al. [9].

2. Theory

2.1. Sound radiated by the flow past a cylinder

As mentioned in Section 1, the aerodynamic noise produced by a circular cylinder in a transverse flow at low Mach numbers can be modelled by the sound radiated by quadrupolar volume sources in the wake that are scattered by the body surface. Although the velocity field behind the body is intrinsically 3-D in the regime investigated in the study, the choice of this 2-D approach can provide an acceptable representation of the flow topology, which is dominated by periodic vortices that alternately detach from opposite sides of the cylinder. Following the notation of Gloerfelt et al. [9], the quantities derived in this section are expressed in the frequency domain. Indeed, the pseudo-periodicity of the vortex shedding makes it possible to solve the problem harmonically and avoids the numerical differentiation of flow quantities, which can hamper the accuracy of the results.

The starting point of the 2-D formulation is the inhomogeneous Helmholtz equation, which, for an observer located at $\mathbf{x}$, reads

$$(\nabla^2 + k_0^2)\,\hat{p}(\mathbf{x},\omega) = \hat{q}(\mathbf{x},\omega). \tag{1}$$

Here, k_0 is the acoustic wavenumber ω/c_0, where ω and c_0 are the angular frequency of the excitation and the mean speed of sound, respectively, $\hat{p}$ is the Fourier transform of the pressure-fluctuation field within the acoustic region, and $\hat{q}$ is the source field. $\hat{p}$ and $\hat{q}$ are defined in a finite volume V containing a surface S (see Fig. 1). Eq. (1) can be solved by means of the convolution product with the frequency-domain Green's function, which, for a point source in $\mathbf{y}$, satisfies

$$(\nabla^2 + k_0^2)\,\hat{G}(\mathbf{x}|\mathbf{y},\omega) = \delta(\mathbf{x}-\mathbf{y}), \tag{2}$$

where δ is the Dirac delta function. Eq. (2) is subjected to the Sommerfeld radiation boundary condition, which ensures that waves are radiated and not absorbed by the sources. Subsequently, the integration by parts and application of Green's theorem yield

$$\hat{p}(\mathbf{x},\omega) = \iiint_V \hat{q}(\mathbf{y},\omega)\,\hat{G}(\mathbf{x}|\mathbf{y},\omega)\,\mathrm{d}V + \iint_S \left[\hat{G}(\mathbf{x}|\mathbf{y},\omega)\frac{\partial\hat{p}(\mathbf{y},\omega)}{\partial y_i} - \hat{p}(\mathbf{y},\omega)\frac{\partial\hat{G}(\mathbf{x}|\mathbf{y},\omega)}{\partial y_\mathrm{i}}\right] n_\mathrm{i}\,\mathrm{d}S, \tag{3}$$

where $\mathbf{n}$ is the inward-pointing normal on S.

The source term $\hat{q}$ can be estimated following Lighthill's analogy [3]:

$$\hat{q} = -\frac{\partial^2\hat{T}_{ij}}{\partial x_i \partial x_j}, \tag{4}$$

where $\hat{T}_{ij}$ is the Fourier transform of Lighthill's stress tensor $T_{ij} = \rho u_i u_j - \sigma_{ij} + (p - c_0^2\rho')\,\delta_{ij}$, with p, ρ, u_i, σ_{ij}, and δ_{ij} being the pressure, density, flow velocity, viscous stress tensor, and Kronecker delta, respectively. The prime symbol $'$ is here used to denote

fluctuations about the mean value. Specifically, T_{ij} accounts for the sound produced by Reynolds stresses, viscosity, and departures from the linear-limit form of the isentropic relation between pressure and density fluctuations in a homogeneous medium. The volume integral in Eq. (3) can now be reformulated by performing integration by parts and moving the partial derivatives from the source to $\hat{G}$. By employing the divergence theorem and exploiting the symmetry property of $\hat{T}_{ij}$, it follows that [9]

$$\hat{p}(\mathbf{x},\omega) = -\iiint_V \frac{\partial^2 \hat{G}}{\partial y_i \partial y_j}\,\hat{T}_{ij}\,\mathrm{d}V + \iint_S \left[\hat{G}\,\frac{\partial\left(\hat{p}\delta_{ij} + \widehat{\rho u_i u_j}\right)}{\partial y_i} - \left(\hat{p}\delta_{ij} + \widehat{\rho u_i u_j}\right)\frac{\partial \hat{G}}{\partial y_i}\right] n_i\,\mathrm{d}S. \tag{5}$$

A high Reynolds number is assumed in the present formulation. In this way, the viscous stresses can be neglected with regard to the pressure fluctuations and Reynolds stresses in the surface integral, which corresponds to a line in 2-D. For a non-vibrating, solid body, $\hat{u}_i$ is zero on the surface due to the no-slip condition, whereas $\partial\hat{p}/\partial n = 0$ on S due to the rigidity condition. Then, Eq. (5) reads

$$\hat{p}(\mathbf{x},\omega) = -\iiint_V \frac{\partial^2 \hat{G}}{\partial y_i \partial y_j}\,\hat{T}_{ij}\,\mathrm{d}V - \iint_S \hat{p}\,\frac{\partial \hat{G}}{\partial y_i}\,n_i\,\mathrm{d}S. \tag{6}$$

Eq. (6) can be solved with any desired $\hat{G}$. Particularly, when the free-field Green's function $\hat{G}_0$ is applied, Curle's solution to Lighthill's analogy [2] is retrieved:

$$\hat{p}(\mathbf{x},\omega) = -\iiint_V \frac{\partial^2 \hat{G}_0}{\partial y_i \partial y_j}\,\hat{T}_{ij}\,\mathrm{d}V - \iint_S \hat{p}\,\frac{\partial \hat{G}_0}{\partial y_i}\,n_i\,\mathrm{d}S. \tag{7}$$

However, a tailored Green's function $\hat{G}_1$ such that $\partial\hat{G}_1/\partial n = 0$ on S can also be prescribed to account for the presence of the body and its acoustic response. This approach makes the surface integral vanish, yielding

$$\hat{p}(\mathbf{x},\omega) = -\iiint_V \frac{\partial^2 \hat{G}_1}{\partial y_i \partial y_j}\,\hat{T}_{ij}\,\mathrm{d}V. \tag{8}$$

Therefore, the problem reduces to finding a suitable expression for $\hat{G}_1$, which may be constructed by adding any solution of the homogeneous Helmholtz equation to the free-field Green's function, i.e. $\hat{G}_1 = \hat{G}_0 + \hat{G}_s$. The latter term allows the boundary condition on the body surface to be verified and includes diffraction effects.

The comparison between Eqs. (7) and (8) suggests that the surface (line in 2-D) integral in Curle's analogy physically corresponds to the component of the aerodynamic noise produced by the volume term (surface in 2-D) that is scattered by the body [9,25]:

$$\iint_S \hat{p}\,\frac{\partial \hat{G}_0}{\partial y_i}\,n_i\,\mathrm{d}S = \iiint_V \frac{\partial^2 \hat{G}_s}{\partial y_i \partial y_j}\,\hat{T}_{ij}\,\mathrm{d}V. \tag{9}$$

The surface term is thus reinterpreted as a different equivalent sound source that maintains a dipolar directivity pattern in the far field.

2.2. Construction of the tailored Green's function

A cylindrical coordinate system $\mathbf{x} = (r_x, \Theta_x)$ and $\mathbf{y} = (r_y, \Theta_y)$ is adopted to model the scattering of sound by a solid circular cylinder with diameter d (see Fig. 1). In such a reference system, $\hat{G}_0$ can be expressed as [26]

$$\hat{G}_0(\mathbf{x}|\mathbf{y},\omega) = \frac{1}{4\mathrm{i}}\sum_{m=0}^{+\infty} \epsilon_m \cos m(\Theta_y - \Theta_x)\, H_m^{(1)}(k_0 r_x)\, J_m(k_0 r_y), \tag{10}$$

where $\epsilon_m = 1$ for $m = 0$ and $\epsilon_m = 2$ otherwise. Here, $H_m^{(1)}$ is the m$^{\text{th}}$-order Hankel function of the first kind and J_m is the m$^{\text{th}}$-order Bessel function.

Concerning the diffraction term $\hat{G}_s$, Gloerfelt et al. [9] modelled it as a series of outward-going waves using Hankel functions of the first kind, obtaining

$$\hat{G}_s(\mathbf{x}|\mathbf{y},\omega) = \frac{1}{4\mathrm{i}}\sum_{m=0}^{+\infty} \epsilon_m \cos m(\Theta_y - \Theta_x)\, A_m\, H_m^{(1)}(k_0 r_y). \tag{11}$$

By imposing $\partial\hat{G}_1/\partial r_y = 0$ at $r_y = d/2$, it follows that

$$A_m = -\frac{J_{m-1}(k_0\,d/2) - J_{m+1}(k_0\,d/2)}{H_{m-1}^{(1)}(k_0\,d/2) - H_{m+1}^{(1)}(k_0\,d/2)}\, H_m^{(1)}(k_0 r_x). \tag{12}$$

Hence, the final expression for $\hat{G}_1$ is given by

$$\hat{G}_1(\mathbf{x}|\mathbf{y},\omega) = \frac{1}{4\mathrm{i}}\sum_{m=0}^{+\infty} \epsilon_m \cos m(\Theta_y - \Theta_x)\left[J_m(k_0 r_y) - \frac{J_{m-1}(k_0\,d/2) - J_{m+1}(k_0\,d/2)}{H_{m-1}^{(1)}(k_0\,d/2) - H_{m+1}^{(1)}(k_0\,d/2)}\, H_m^{(1)}(k_0 r_y)\right] H_m^{(1)}(k_0 r_x). \tag{13}$$

In Section 4.3, Eq. (8) will be integrated for the case of a simplified quadrupolar source to model the noise-generation mechanism of a circular cylinder coated with a porous material at the vortex-shedding frequency.

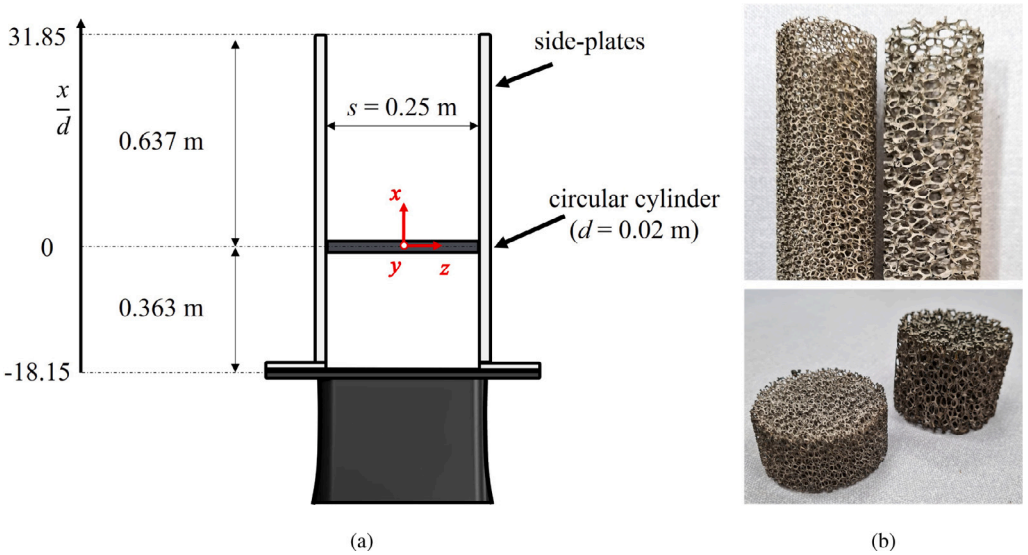

Fig. 2. (a) Test section showing the outlet nozzle, side plates, and cylindrical specimen, including the reference system considered for presenting the results. (b) Picture of the two metal-foam coatings used in the measurement campaign (at the top) and samples employed to characterise the porous medium (at the bottom).

3. Materials and methods

3.1. Wind tunnel facility and cylindrical specimen

The experiments have been performed at the A-tunnel facility of the Delft University of Technology (TU Delft). This is a vertical open–jet wind tunnel located in an anechoic chamber featuring a cutoff frequency of 250 Hz and equipped with Flamex Basic acoustic absorbing foam. A detailed description of its design and main features is provided by Merino-Martínez et al. [27]. The outlet nozzle of the wind tunnel is flush-mounted at the exit of the contraction. It features a rectangular exit plane with a contraction ratio of 42 to 1, a span of $s = 0.250\,\mathrm{m}$, and a width of $w = 0.400\,\mathrm{m}$. Two side plates guide the flow from the outlet nozzle and support the cylindrical specimens having a length equal to s. A sketch of the setup is depicted in Fig. 2(a), where the reference system adopted for the presentation of the results is also indicated. In particular, the x-axis is aligned with the flow direction, the z-axis is aligned with the spanwise direction of the body, and the y-axis is oriented in the normal direction to form a right-handed coordinate system. The origin is set at the centre of the cylinder.

Three configurations have been tested: a bare cylinder as a baseline and two cylinders covered with porous materials characterised by different properties, as will be explained in Section 3.2. The diameter d of the inner cylinder has been kept constant to model a scenario in which external material is added to an existing device. Therefore, the outer diameter D of the coated cylinder differs from that of the baseline and is determined by the thickness of the cover t, according to $D = d + 2t$. The geometry of the specimens has been subsequently designed to meet the following criteria: (i) the aspect ratio of the cylinder, i.e. the ratio of the length to the diameter, shall be larger than 7 to allow the vortex-shedding instability to develop undisturbed [28], justifying the use of a 2-D theory to model the associated noise; (ii) the cylinder diameter shall be sufficiently small with respect to the test section to minimise the blockage exerted by the body, i.e. the ratio of the projected frontal area of the body to the cross-sectional area of the test section should be lower than 5%; (iii) the vortex-shedding frequency f_{VS}, determined by $f_{\mathrm{VS}} \approx 0.2\,U_\infty/d$, U_∞ being the free-stream flow velocity, shall be above the cutoff frequency of the anechoic facility; (iv) t shall be large enough to allow the installation of the porous coating while maintaining its structural integrity. The latter condition is linked to the average pore size of the medium. The resulting dimensions were $d = 20\,\mathrm{mm}$, $D = 30\,\mathrm{mm}$, and $t = 5\,\mathrm{mm}$, leading to aspect ratios of $L/d = 12.5$ and $L/D = 8.33$.

The measurements have been carried out at free-stream flow velocities in the sub-critical regime ranging from $U_\infty = 25\,\mathrm{m\,s^{-1}}$ to $U_\infty = 70\,\mathrm{m\,s^{-1}}$, which correspond to Reynolds numbers based on the inner cylinder diameter of $Re_d = 3.4 \times 10^4$ and $Re_d = 9.5 \times 10^4$, respectively. The flow velocity was estimated through a Pitot static tube connected to a Mensor DPG 2400 pressure gauge featuring accuracy of 0.03% of the read value. The full qualification of the outlet nozzle has already been performed by Merino-Martínez et al. [27], who found that the mean velocity in the streamwise direction was uniform within 0.6% independently of the free-stream speed, while the turbulence intensity of the clean inflow was below 0.1% for the entire range of operative velocities.

3.2. Characterisation of the porous media

The porous coatings are made of two different types of Nickel Ni open-cell metal foams manufactured through the electrodeposition of pure Nickel on a polyurethane foam, which results in a homogeneous micro-structure based on a dodecahedron-shaped cell.

Table 1
Measured properties for the two metal-foam samples. Quantities in square brackets refer to the nominal values provided by the manufacturer.

PPI (–)	φ (%)	R (N s m^{-4})	K (m^2)	C (m^{-1})
[30]	[80]	1.296×10^2	1.390×10^{-7}	1.834×10^2
[10]	[95]	4.148×10^1	4.371×10^{-7}	1.103×10^2

This material has already been deployed for similar experimental campaigns [12,19,29]. The two metal foams feature a nominal cell diameter of 30 PPI and 10 PPI, where PPI is a non-SI unit typically used as an index for the number of pores per inch, and a porosity φ, defined as the ratio of the void volume to the total volume, of 80% and 95%, respectively. These values have been chosen following the studies reported in the literature. A picture of the two materials is shown in Fig. 2(b).

The characterisation of the porous media has been carried out using the experimental rig designed by Rubio Carpio et al. [30]. The method consists of least-squares fitting the measurements of the pressure drop Δp across a homogeneous porous material sample with thickness t_s to the Hazen–Dupuit–Darcy quadratic equation, defined as [31]

$$\frac{\Delta p}{t_s} = \frac{\mu}{K} v_d + \rho C v_d^2, \tag{14}$$

where μ is the fluid dynamic viscosity, v_d is the Darcian velocity, which is determined as the ratio of the volumetric flow rate to the cross-section area of the material sample, and K and C are the static permeability and form coefficient of the porous medium, which account for pressure losses due to viscous and inertial effects, respectively. The term $R = \Delta p/(t_s\, v_d)$ also denotes the static air-flow resistivity of the material. A total of 20 values of pressure drop, corresponding to Darcian velocities ranging between 0 m s^{-1} and 2.5 m s^{-1}, were employed for fitting Eq. (14).

Pressurised air supplied the experimental rig. Two ports were located 50 mm upstream and downstream of the test section and connected to a Mensor DPG 2101 pressure gauge having an accuracy of 2 Pa. The volumetric flow rate was controlled through an Aventics pressure regulator and evaluated by a TSI 4040 volumetric flow meter, which was placed upstream of the pipe and featured an accuracy of 2% of the read value.

The porous samples were 55 mm metal-foam disks (see Fig. 2(b)) inserted in a hollow aluminium cylinder that was located in the test section. t_s has been varied between 25 mm and 100 mm and between 40 mm and 120 mm for the 30 PPI and 10 PPI metal foam, respectively, to study the occurrence of entrance or exit effects on the measured pressure drop, which may prevail if the thickness of the sample is smaller or comparable to the pore diameter [32,33]. Convergence of the values for K and C has been found for the thickest samples. The results of the characterisation are listed in Table 1 and show that the larger the cell diameter of the porous medium is, the higher the static permeability and the lower the static air-flow resistivity and the form coefficient are. These parameters provide a detailed description of the metal foam considered in the paper and can be used to calibrate porous models in numerical simulations of the present experimental setup.

3.3. Far-field acoustic measurements

An array of 64 G.R.A.S. 40 PH analogue free-field microphones with integrated constant-current power amplifiers has been employed for the far-field acoustic measurements. Each sensor features a diameter of 0.007 m and a length of 0.059 m, and is characterised by a flat frequency response within ±1 dB from 50 Hz to 5 kHz and within ±2 dB from 5 kHz to 20 kHz. The transducers are connected to a data acquisition system consisting of 4 NI PXIe-4499 Sound and Vibration modules having a 24-bit resolution and a 204.8 kHz maximum sampling rate. The modules are controlled by a NI RMC-8354 computer via a NI PXIe-8370 board. All the microphones are calibrated in amplitude using a G.R.A.S. 42AG piston-phone, which emits a sinusoidal wave with an amplitude of 94 dB at 1 kHz.

The array has an aperture D_a of approximately 2 m and is arranged in an optimised multi-arm spiral configuration [34] placed parallel to the $x - z$ plane. With respect to the reference system introduced in Section 3.1, the central microphone is placed at $(x, y, z) = (2.5\,d,\ 50\,d,\ -0.75\,d)$. A sketch of the relative position of the microphone array and the test section is illustrated in Fig. 3(a). With the present setup, the minimum resolvable source separation R is given by the Rayleigh criterion [35] as

$$R(f) \approx d_{\mathrm{a-c}} \tan\left(\frac{1.22\, c_\infty}{f\, D_a}\right), \tag{15}$$

where $d_{\mathrm{a-c}}$ is the distance between the microphone array and the cylinder centre, i.e. 1 m, and f is the investigated frequency. For each configuration, data have been acquired at a sampling frequency of 102.4 kHz for 20 s. A total of 7 free-stream Reynolds numbers have been considered, namely $Re_d = 3.4 \times 10^4,\ 4.1 \times 10^4,\ 4.8 \times 10^4,\ 5.4 \times 10^4,\ 6.8 \times 10^4,\ 8.2 \times 10^4$ and 9.5×10^4.

The power spectra of the measured acoustic signals have been computed using the Welch method [36] with blocks of 2^{13} samples, corresponding to 0.16 s, windowed through a Hanning weighting function having a 50 % data overlap, thus resulting in a frequency resolution of 6.25 Hz. For these parameters, the associated random error, considering a 95% confidence interval, is estimated to be in the order of 0.8 dB [37]. Moreover, to visualise the noise sources, the data have been processed through an in-house conventional frequency-domain beamforming technique [38,39]. In this case, the sound propagation from each potential source to every listener location, i.e. every microphone, is modelled by means of the free-field Green's function. Furthermore, corrections to account for the convection of the mean flow and refraction of the shear layer have been applied following the method proposed by Sijtsma [40],

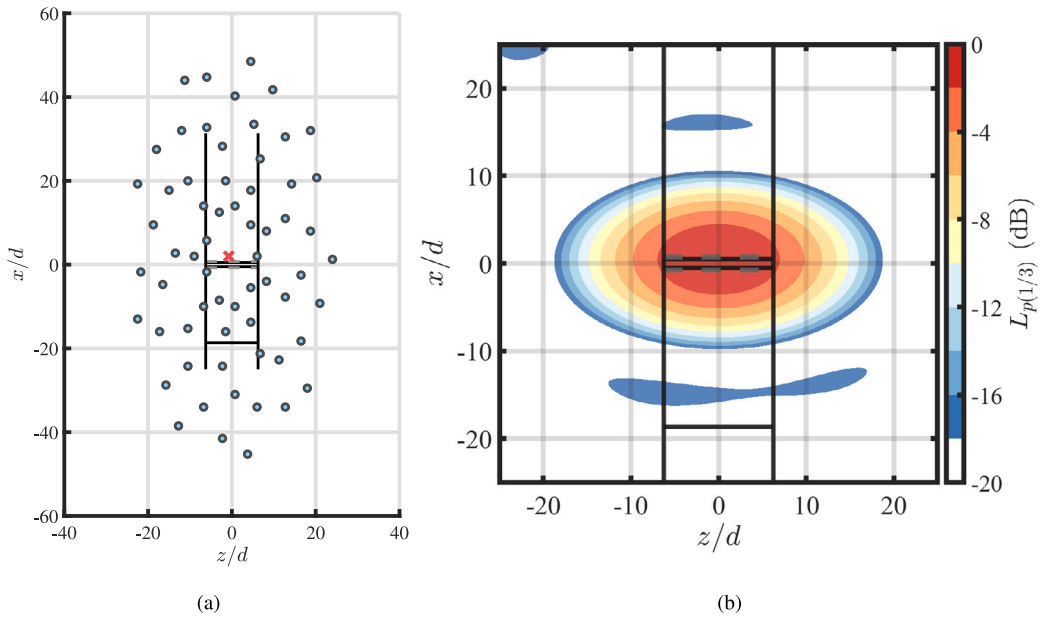

Fig. 3. (a) Relative position of the microphone array and the test section. The solid lines indicate side plates, nozzle exit, and cylinder leading edge and trailing edge. The central microphone of the array is denoted by the red x symbol. (b) Point-spread function at $f_{1/3} = 1.25\,\mathrm{kHz}$ for a simulated source emitting white noise at the origin of the coordinate system. The flow goes from the bottom to the top of the maps.

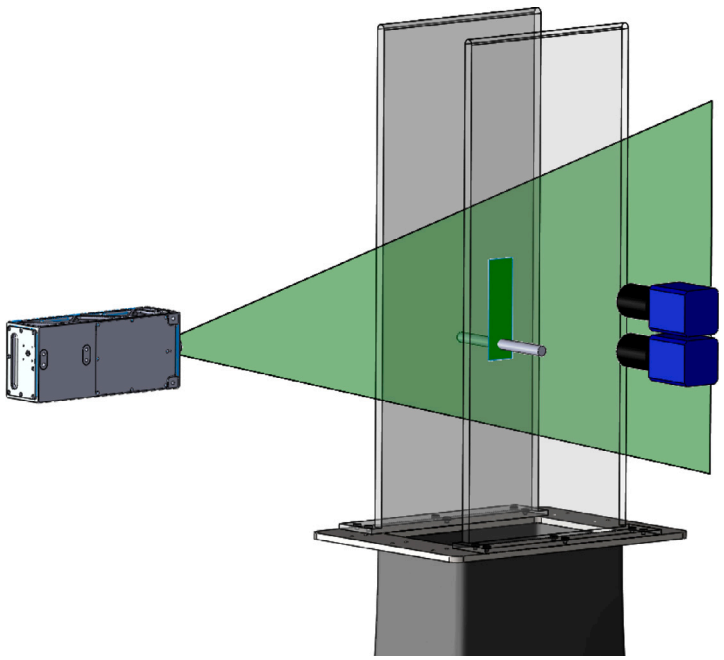

Fig. 4. Sketch of the 2C-PIV setup arranged for the experimental campaign. The positions of the cameras, laser head, laser sheet, and FOV with respect to the bare cylinder are shown.

whereas measurements of the test section without the cylindrical specimens have been taken to assess the background noise of the facility.

The scanning grid for the evaluation of the potential sources ranges between $-25 < z/d < 25$ and $-25 < x/d < 25$, with a spatial resolution of $0.25\,d$, and is centred at the origin of the reference system. The extension of the grid can be observed in Fig. 3(b), which shows the point-spread function of the array [38] for a synthetic point source placed at the origin and emitting white noise at

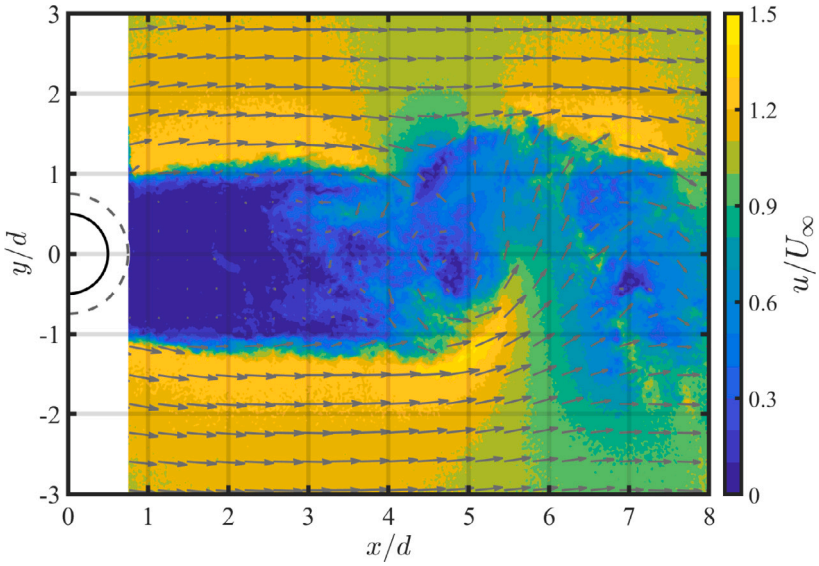

Fig. 5. Instantaneous-velocity-magnitude field for the cylinder coated with the 30 PPI metal foam measured at $Re_d = 6.8 \times 10^4$. A mask to neglect the shadow region shed by the cylinder has been applied.

Table 2
Free-stream flow speeds tested for each measurement type.

Measurement type	U_∞ (m s^{-1})						
Phased-microphone array	25	30	35	40	50	60	70
2C-PIV	–	30	–	40	50	–	–

the one-third octave frequency band of $f_{1/3} = 1.25$ kHz. As revealed by the resulting sound map, the point-spread function features axial symmetry with respect to the x and z axes and is characterised by a higher resolution along x, making the array particularly suitable to separate noise sources in the streamwise direction.

3.4. PIV measurements

Two-component (2C) PIV experiments have been performed on a x–y plane at the midspan of the cylinder, centred in the wake region of the body. 2 LaVision Imager sCMOS camera having a sensor of 2560 px × 2160 px and pixel pitch of 6.5 μm have been placed at approximately 75 d from the measurement plane and equipped with Nikon NIKKOR 105 mm focal-distance macro-objectives set at $f_\# = 11$. Scheimpflug adapters have been installed on each camera to account for misalignment angles minor than 5°. Seeding has been produced by a SAFEX Twin-Fog Double Power fog generator with a SAFEX Long-Lasting glycol mix. Particles with mean drop diameters of 0.5 μm have been introduced in the wind tunnel circuit to grant a uniform concentration while recirculating in the test section. The laser sheet has been obtained through laser pulses with a wavelength of 532 nm and energy of 200 μJ per pulse that are generated by a Quantel Evergreen EVG00200 double-pulse Nd:YAG system, resulting in an approximate thickness of 1 mm. A sketch of the 2C-PIV setup is depicted in Fig. 4.

Sets of 2000 uncorrelated image pairs have been acquired at a sampling frequency of 10 Hz for each configuration at free-stream Reynolds numbers of $Re_d = 4.1 \times 10^4$, $Re_d = 5.4 \times 10^4$, and $Re_d = 6.8 \times 10^4$. A summary of the tested flow speeds per each measurement type is listed in Table 2. The separation time between two frames has been adapted to maintain a pixel displacement in the free stream of about 12 px. The combined field of view (FOV) has a dimension of 8.1 d × 13.2 d and a digital resolution of 13.9 px mm^{-1} (magnification factor: 0.087), as can be seen in Fig. 5, which depicts an instantaneous velocity-magnitude field reconstructed for the cylinder coated with the 30 PPI metal foam at $Re_d = 6.8 \times 10^4$.

The processing of the raw images has been carried out with the commercial software LaVision Davis 10.1.2 employing a multi-pass cross-correlation approach [41] with a final interrogation window of 16 px × 16 px and 75% overlapping, which leads to a spatial resolution of 0.06 d × 0.06 d and a vector spacing of 0.015 d × 0.015 d.

The overall systematic and random components of PIV uncertainty can be determined with a method based on a statistical analysis of the correlation process that evaluates the differences in the correlation peaks computed from a pair of interrogation windows mapped back onto each other [42]. The uncertainty results from averaging the residuals coming from the image mapping with the technique of Sciacchitano and Wieneke [43]. The outcome indicates a maximum error on the mean-velocity magnitude below 0.02 U_∞ for all the Reynolds numbers considered in the study.

For processing the results, the sets of 2000 snapshots have been ensemble-averaged to retrieve the statistics of the flow field. Moreover, the Γ_1 and Γ_2 scalar functions, which are based on the normal angular momentum of the instantaneous velocity field, have been employed to identify the large-scale vortical structures in the wake of the cylinders [44]. The former is equivalent to a spatial pulse whose peak value represents the sign ± 1 of vorticity at the cores of the turbulent structures and decays fast when moving away from them. The latter allows the regions dominated by the rotation rate to be separated from those dominated by the strain rate and, by doing so, provides the shape of the large vortical structures independently of their strength. Following Graftieaux et al. [44], they are defined as

$$\Gamma_1(\mathbf{x}_P) = \frac{1}{N} \sum_{S_P} \frac{[(\mathbf{x}_P - \mathbf{x}_M) \times \mathbf{u}_M] \cdot \mathbf{n}_P}{(\mathbf{x}_P - \mathbf{x}_M) \cdot \mathbf{u}_M}; \tag{16}$$

$$\Gamma_2(\mathbf{x}_P) = \frac{1}{N} \sum_{S_P} \frac{[(\mathbf{x}_P - \mathbf{x}_M) \times (\mathbf{u}_M - \overline{\mathbf{u}}_P)] \cdot \mathbf{n}_P}{(\mathbf{x}_P - \mathbf{x}_M) \cdot (\mathbf{u}_M - \overline{\mathbf{u}}_P)}, \tag{17}$$

where P is a fixed point at the position $\mathbf{x}_P$, S_P is a discretised 2-D area surrounding P and containing N points, $\mathbf{n}_P$ is the unit-vector outward-pointing normal to S_P, and $\mathbf{u}_M$ and $\overline{\mathbf{u}}_P$ are the instantaneous velocity at the generic point M and local convection velocity at the point P, respectively. The separation between the regions of dominant rotation rate and strain rate occurs for $|\Gamma_2| = 2/\pi$. The size of the area, i.e. the parameter N, plays the role of a spatial filter and is set to be $0.5\,d \times 0.5\,d$ wide in the present study.

4. Results and discussion

4.1. Aeroacoustic results

The sound pressure levels L_p of the signal measured by the central microphone of the array are illustrated in Fig. 6 for the three configurations and different free-stream Reynolds numbers. The results, a preliminary version of which has been reported by Zamponi et al. [24], are calculated with a reference acoustic pressure of $p_{\text{ref}} = 20$ μPa and presented as a function of the Strouhal number based on d and U_∞. Overall, the porous coatings are effective in reducing noise, with a trend that is independent of the flow velocity. The difference in the outer diameter of the coated cylinder results in a shift of the tonal peak associated with the vortex shedding at $St_{\text{VS}} = 0.185$ towards lower frequencies and significant suppression of its amplitude, with peak-to-peak reductions of up to 30 dB. In accordance with the papers reviewed in Section 1, the bandwidth of this tone is found to be narrowed, possibly because the turbulent mixing in the near wake is initiated downstream by a weaker shedding, and the communication between the shear layers is more balanced. The Strouhal number of the vortex-shedding instability for the baseline agrees with previous measurements involving circular cylinders tested in the same experimental setup [45]. An analogous value of $St_{\text{VS}} = 0.185$ would be retrieved for the 30 PPI coating if the acoustic spectra were scaled using an equivalent solid diameter of $D_{\text{eq}} = 1.027\,D$, whereas a value of $D_{\text{eq}} = 0.950\,D$ would be required to achieve the same result for the 10 PPI one. Indeed, the high static permeability of the latter configuration most likely changes the equivalent diameter of the covered cylinder, influencing the flow penetration.

In addition, the 30 PPI metal foam is more efficient than the 10 PPI one in suppressing the L_p peak of the vortex-shedding frequency. Interestingly, the sound pressure levels measured at this frequency are exceeded by those evaluated at its first harmonic for the 30 PPI case, which is substantially more preponderant than for the baseline. According to the standard view of the problem, the first harmonic is usually linked to the drag fundamental frequency, whose corresponding equivalent source is expected to be oriented parallel to the streamwise direction and has a considerably smaller influence on the radiated sound in the crosswise one, where the microphones of the array are placed. The porous coating possibly alters the relative weight of the scattered sources at these frequencies, but further investigations would be required to clarify these phenomena.

Two different trends define the broadband-noise range. On the one hand, for $St < 1$, a significant attenuation of up to 10 dB is achieved, and no clear distinction can be observed between the two metal foams. This result supports a scenario in which the sound-reduction mechanism acting in such a frequency range is not directly linked to the porosity and permeability of the porous medium. On the other hand, for $St > 1$, the coated configurations start diverging, likely due to the inner turbulent flow interacting with the struts of the open-cell metal foam [46]. This noise source is more relevant and emerges at lower frequencies for the most permeable cover since the larger average pore size of the material allows more flow to permeate the medium. This effect, in turn, lowers the aeroacoustic performance of the porous treatment at higher frequencies, with noise increments of up to 10 dB.

In Fig. 7, the sound pressure levels are scaled with the sixth power of the Mach number M, which is typically associated with a dipolar source [2]. At this observation angle, i.e. at $\Theta = \pi/2$ with reference to Fig. 1, a satisfactory collapse of the spectra is obtained for the baseline (Fig. 7(a)) up to $St \approx 1$. This finding is in agreement with the literature [8] and suggests that the noise measured by the central microphone of the array is predominantly dipolar in nature, i.e. as scattered by a solid body (see Section 1). The coated configurations (Figs. 7(b) and 7(c)) exhibit a similar trend, although the scaling with M^6 appears to be not as good as for the bare cylinder, especially at $St > 1$. The lack of collapse for this frequency range implies that the corresponding noise-generation mechanism is different, confirming the connection with the turbulent-flow interaction within the pores of the permeable covers indicated above. A further hypothesis for the failure in the scaling with the sixth power of the Mach number is attributable to the non-compactness of the body at high frequencies, which would additionally clarify the absence of collapse occurring at high Strouhal numbers.

A more quantitative assessment of the dependency of the sound spectra with the Mach number for the different configurations is provided in Figs. 8 and 9, which illustrate the variation over the free-stream Reynolds number of the overall sound pressure level

$$L_{p_0} = 10 \log_{10} \left(\sum 10^{L_p/10\,\text{dB}} \right) \text{dB} \tag{18}$$

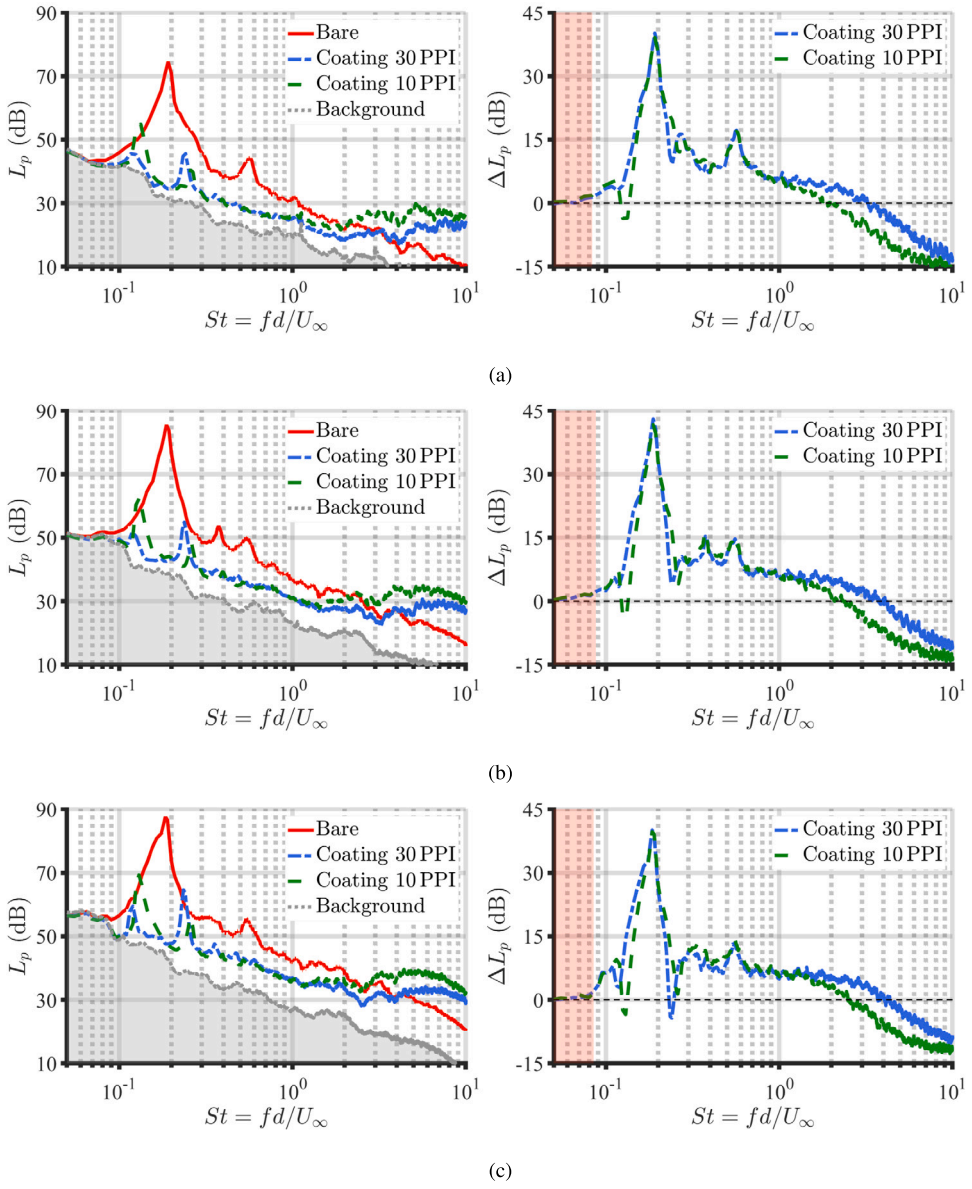

Fig. 6. Absolute and relative sound pressure levels for the different configurations at (a) $Re_d = 4.1 \times 10^4$, (b) $Re_d = 5.4 \times 10^4$, and (c) $Re_d = 6.8 \times 10^4$ measured by the central microphone of the array and computed with $p_{\text{ref}} = 20$ μPa. The dashed horizontal lines in the ΔL_p plots indicate the trade-off between noise increase and decrease, while the tinted areas denote the regions in which the signal-to-noise ratio for the baseline is lower than 3 dB.

evaluated at the central microphone of the array and at the most downstream one ($x/d \approx 50$ considering Fig. 3(a)), respectively. Two separate integrations have been performed to evaluate the scaling of the tonal and broadband components of the frequency spectrum. The former encompasses a range of $\Delta St = 0.15$ centred at the Strouhal number linked to the vortex-shedding frequency to avoid contamination from the background noise. The latter focuses on the St range that extends from the upper end of the range for the tonal contribution analysed above to the frequency at which the noise associated with the turbulent-flow interaction within the pores starts occurring. It is important to specify that, for both components, the L_{p_0} amplitudes of the different cylinders cannot be directly compared since the vortex-shedding frequency, as well as the frequency at which the onset of the high-frequency noise occurs, differ depending on the considered configuration.

For the central microphone, the results related to the tonal component (Fig. 8(a)) confirm a L_{p_0} dependency close to M^6 for the baseline, as deduced from Fig. 7(a). Interestingly, a somewhat different trend characterises the covered cylinders. For the 10 PPI cover, the power with which the spectra scale with the Mach number appears to be higher than 6, more precisely in the order of 6.6. This tendency is even more pronounced for the 30 PPI coating, for which the scaling coefficient is found to be approximately 6.9. It follows that, while the radiated sound can be considered purely dipolar for the bare cylinder, the directivity of the noise induced

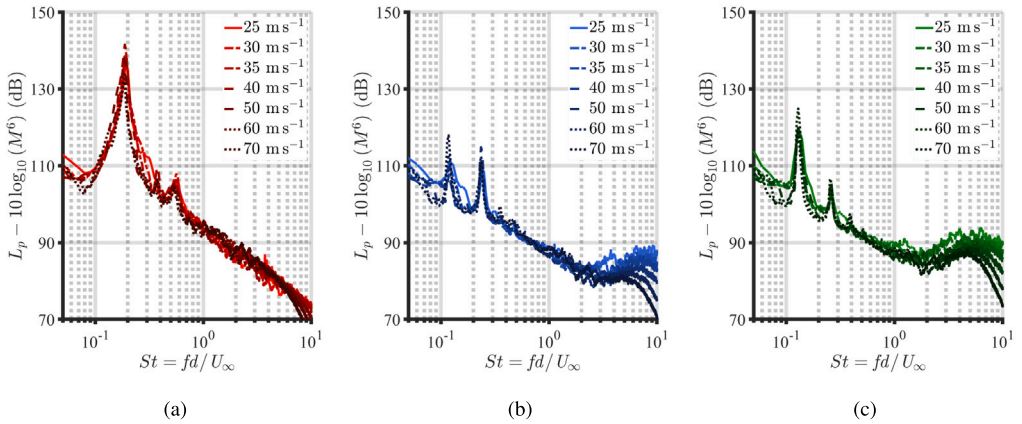

Fig. 7. Sound pressure levels at different free-stream flow velocities for (a) the baseline and the cylinders coated with the (b) 30 PPI and (c) 10 PPI metal foams measured by the central microphone of the array and computed with $p_{ref} = 20$ μPa. The spectra are scaled with the sixth power of the Mach number.

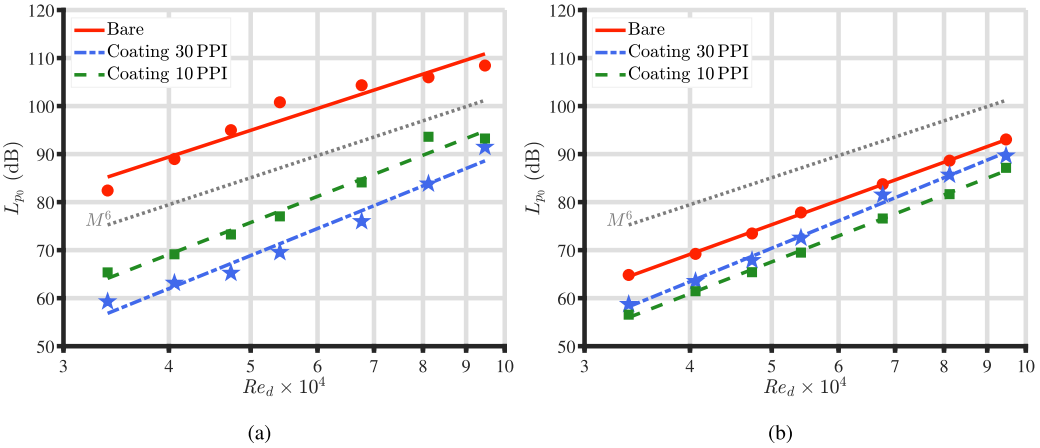

Fig. 8. Overall sound pressure levels ($p_{ref} = 20$ μPa) of the (a) tonal and (b) broadband part of the frequency spectrum at different free-stream Reynolds numbers for the three configurations measured by the central microphone of the array. The slope associated with the sixth power of the Mach number, as well as the interpolation of the experimental points using a linear regression model, are also indicated in the plot.

by the coated configurations features a more complex pseudo-dipolar pattern. Similar trends are also observed for the broadband component (Fig. 8(b)), yet with a slight increase in the scaling coefficients for all the cases (about 6.3, 7.2, and 6.8 for the baseline and the cylinders coated with the 30 PPI and 10 PPI metal foam, respectively).

Notably, the scaling coefficients for the three configurations start diverging even further from the M^6 law when the downstream microphone is considered. For the tonal component (Fig. 9(a)), values of approximately 6.4, 7.7, and 7.1 are retrieved for the baseline and the configurations equipped with the 30 PPI and 10 PPI covers, respectively. Similarly to the case for the central microphone, these scaling coefficients increase to about 6.5, 7.8, and 7.2 for the broadband component (Fig. 9(b)). The topic will be explored in more detail in Section 4.3.

The dominant sound sources produced by the flow past the cylinders are now localised with acoustic beamforming. Source-distribution maps at different one-third octave frequency bands varying in the broadband-noise region of the spectrum are illustrated in Figs. 10–13 using a dynamic range of 10 dB. For all the considered bands, the one-third octave sound pressure levels $L_{p(1/3)}$ generated by the cylinders were found to lie well above the noise floor of the beamformer. The results for the three configurations are presented for $Re_d = 6.8 \times 10^4$, but the discussions made below can also be generalised to the other free-stream flow velocities.

At $f_{1/3} = 1.25$ kHz (Fig. 10), corresponding to $St = 0.5$, the dominant noise sources for the baseline are found in the proximity of the trailing edge. Interestingly, those for the coated configurations are shifted further downstream. The physical interpretation of these sound maps will be discussed in more detail in Section 4.3 with the aid of the theoretical framework outlined in Section 2. Moreover, the downstream source shift is more prominent for the 30 PPI case, for which the peak is centred at $x/d \approx 5$, i.e. $x/D_{eq} \approx 3.2$, than for the 10 PPI one, for which the dominant sources are located at $x/d \approx 4$, i.e. $x/D_{eq} \approx 2.8$. This effect cannot possibly be produced by scattering effects from the side plates. Indeed, the presence of a reflective planar surface would induce an image source positioned on its normal, which is oriented along the spanwise direction.

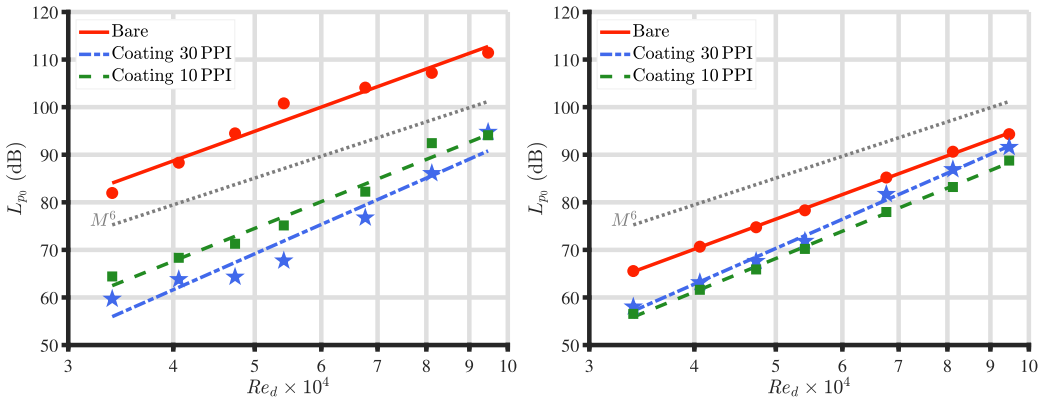

Fig. 9. Overall sound pressure levels ($p_{ref} = 20$ μPa) of the (a) tonal and (b) broadband part of the frequency spectrum at different free-stream Reynolds numbers for the three configurations measured by the most downstream microphone of the array. The slope associated with the sixth power of the Mach number, as well as the interpolation of the experimental points using a linear regression model, are also indicated in the plot.

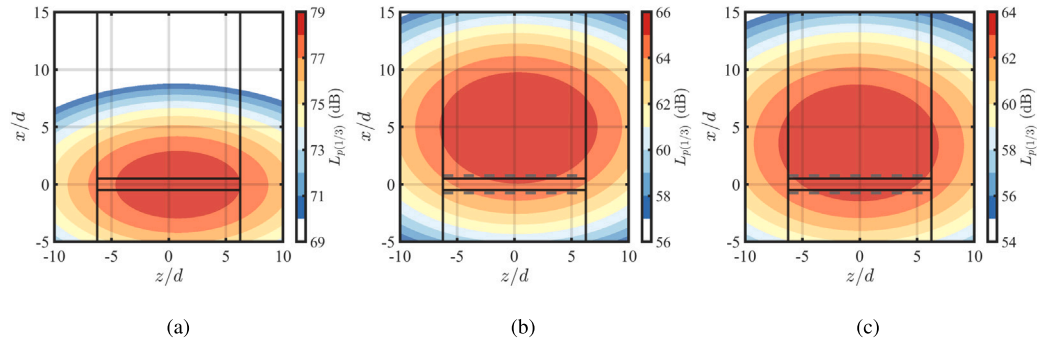

Fig. 10. Source-distribution maps for (a) the baseline and the cylinder coated with the (b) 30 PPI and (c) 10 PPI metal foams at $f_{1/3} = 1.25$ kHz and $Re_d = 6.8 \times 10^4$ ($St = 0.5$) computed with $p_{ref} = 20$ μPa.

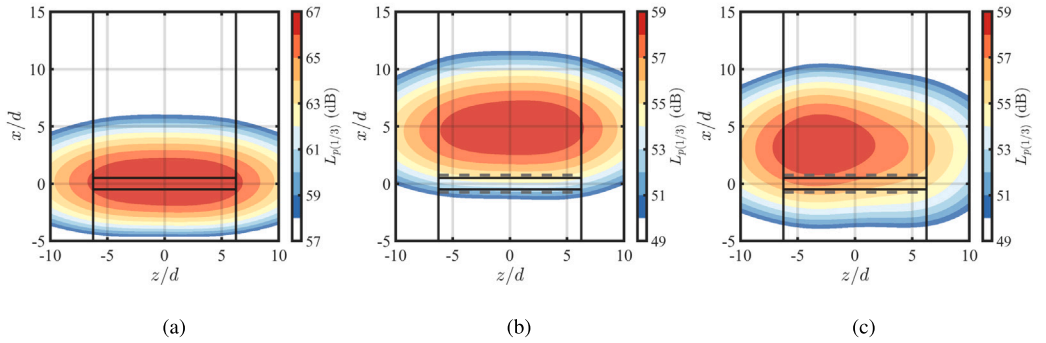

Fig. 11. Source-distribution maps for (a) the baseline and the cylinders coated with the (b) 30 PPI and (c) 10 PPI metal foams at $f_{1/3} = 2.5$ kHz and $Re_d = 6.8 \times 10^4$ ($St = 1$) computed with $p_{ref} = 20$ μPa.

The same conclusions can be drawn for $f_{1/3} = 2.5$ kHz (Fig. 11), corresponding to $St = 1$. In this case, the source regions exhibit a more defined distributed nature in the spanwise direction thanks to the higher spatial resolution of the beamforming method at increased frequencies (see Eq. (15)). The position of the dominant noise sources for the different configurations is consistent with the lower Strouhal number, demonstrating that the physical mechanisms at the basis of the downstream source shift are independent of the frequency. Interestingly, the sound map for the 10 PPI metal foam features a considerably higher concentration close to the

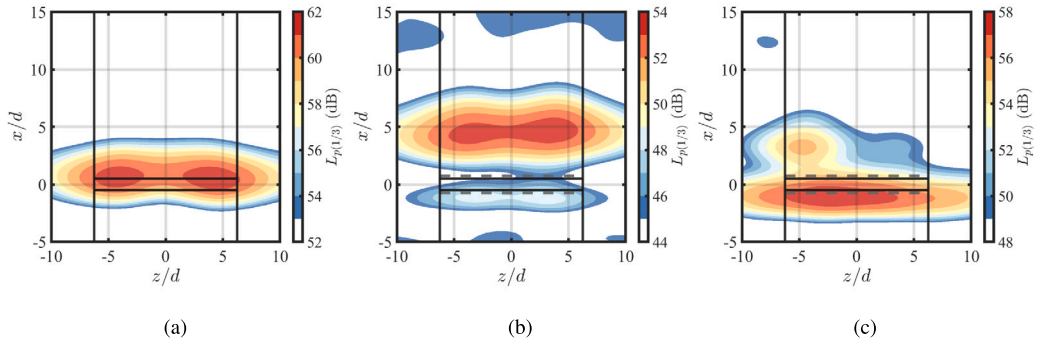

Fig. 12. Source-distribution maps for (a) the baseline and the cylinders coated with the (b) 30 PPI and (c) 10 PPI metal foams at $f_{1/3} = 5$ kHz and $Re_d = 6.8 \times 10^4$ ($St = 2$) computed with $p_{ref} = 20$ μPa.

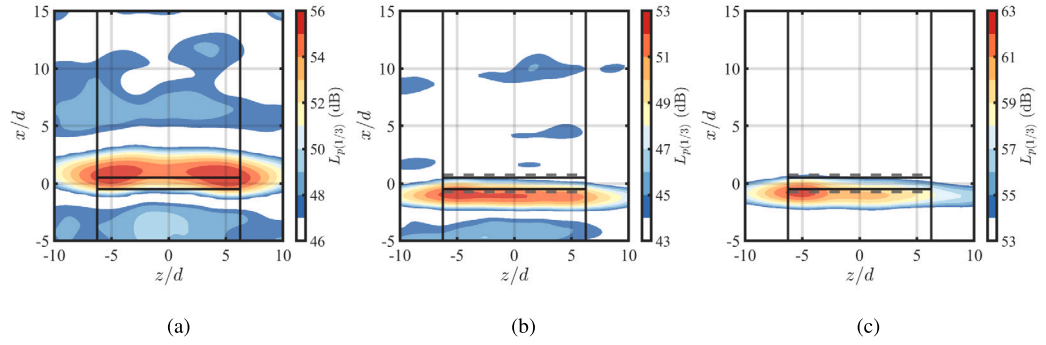

Fig. 13. Source-distribution maps for (a) the baseline and the cylinders coated with the (b) 30 PPI and (c) 10 PPI metal foams at $f_{1/3} = 8$ kHz and $Re_d = 6.8 \times 10^4$ ($St = 3.2$) computed with $p_{ref} = 20$ μPa.

left side plate, which may be attributable to non-homogeneity in the permeable material that alters the associated noise-production mechanism.

At $f_{1/3} = 5$ kHz (Fig. 12), corresponding to $St = 2$, the trends for the two coated cylinders change. While the dominant noise sources are distributed along the span in the vicinity of the trailing edge and at $x/d \approx 5$ for the baseline and the 30 PPI case, respectively, the sound is predominantly coming from the leading edge of the specimen for the 10 PPI case, although traces of non-negligible acoustic energy are still present in the body wake. This displacement is due to the emergence of noise linked to the turbulent-flow interaction within the pores. Such an outcome agrees with the sound pressure levels in Fig. 6, which shows that the alteration in the slope of the L_p spectra in the broadband region, i.e. the Strouhal number at which this noise source starts dominating, takes place within $2 < St < 2.5$ and $1 < St < 1.5$ for the 30 PPI and 10 PPI metal foam, respectively.

The nature of the high-frequency noise increase due to the porosity can be further investigated in the sound maps computed at $f_{1/3} = 8$ kHz (Fig. 13), corresponding to $St = 3.2$. At this frequency, the location of the dominant noise sources is unchanged for the baseline, yet with a higher spatial resolution, whereas it shifts towards the leading edge for the cylinder coated with the 30 PPI metal foam. For the 10 PPI case, the sound-source distribution is consistent with that at $f_{1/3} = 5$ kHz, even though the contribution of acoustic energy in the wake falls outside of the considered dynamic range in this case. The results corroborate the hypothesis that the noise increase is connected with the fluid–structure interactions of the internal flow field with the metal-foam pores at the position where the transpiration velocity is the largest.

The findings discussed above indicate that a consistent downstream source shift occurs for all the analysed frequencies in the broadband-noise range. It is now essential to question whether this phenomenon extends to the tonal component of the noise spectrum. Given the particularly low frequencies at which vortex shedding takes place and the architecture of the microphone array employed in the measurement campaign, the source localisation achievable with acoustic beamforming is characterised by limited spatial resolution and accuracy. Besides, the distance between the dominant noise region in the wake for the covered cylinders and the body surface is considerably lower than the minimum resolvable distance given by the Rayleigh criterion in Eq. (15). Nevertheless, the displacement experienced by the dominant source region can still be qualitatively visualised when the highest flow speed is targeted, as shown in Fig. 14, which depicts the beamforming sound maps of the three configurations computed at the corresponding vortex-shedding narrow frequency for $Re_d = 9.5 \times 10^4$. In this case, f is set to 650 Hz for the bare cylinder and to 400 Hz and 450 Hz for the cylinders coated with the 30 PPI and 10 PPI metal foam, respectively. The outcome of this investigation is, within the resolution of the method, coherent with what is seen in Fig. 10. For the baseline, the dominant source distribution appears

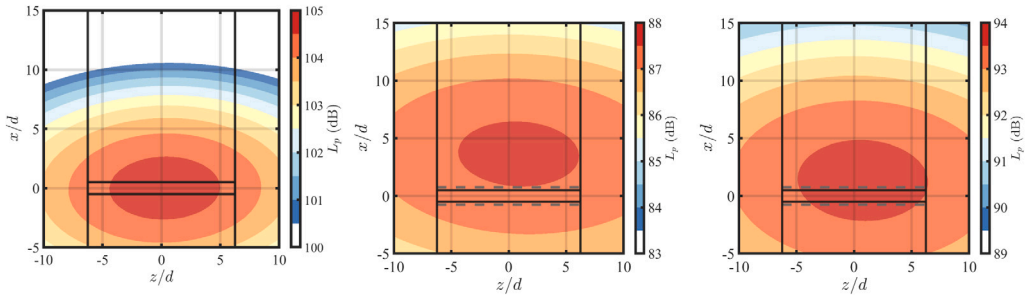

Fig. 14. Source-distribution maps evaluated at the corresponding vortex-shedding frequencies at $Re_d = 9.5\times10^4$ for (a) the baseline ($f = 650$ Hz) and the cylinders coated with the (b) 30 PPI ($f = 400$ Hz) and (c) 10 PPI ($f = 450$ Hz) metal foams computed with $p_{ref} = 20$ μPa. The dynamic range is reduced to 5 dB to ease the visualisation of the maps.

to be centred in the aft part of the body, while, for the covered cylinders, a downstream shift occurs, even though it appears less pronounced than in the broadband range. In particular, the dominant noise sources in the sound maps for the coated configurations extend from the cylinder surface to the near-wake region. A thorough explanation of these results will be provided in Section 4.3.

4.2. Aerodynamic results

The analysis of the flow-field alterations due to porosity can explain the outcome of the aeroacoustic investigation. A preliminary version of these results has been recently presented by the authors [24]. The mean streamwise velocity $\overline{u}_x$, mean spanwise vorticity Ω_z, different components of the Reynolds-stress tensor defined as $\tau'_{ij} = \overline{u'_i u'_j}$, and turbulence kinetic energy $k = 0.5\,(\overline{u'_x} + \overline{u'_y})$ are shown in Figs. 15, 17 and 18 for the three configurations. All the values are normalised with U_∞ and/or d. Even in this case, the plots refer to $Re_d = 6.8\times10^4$, but equivalent considerations can be extended to the other free-stream Reynolds numbers.

One of the prominent effects of the porous coating on the velocity field is to widen the cylinder wake through the re-injection of low-energy fluid past the body [17] that, in turn, affects the flow pattern where the shedding instability develops. As a consequence, the flow is stabilised, and the recirculation zone in the wake, which is located close to the body surface for the baseline (Fig. 15(a)), moves further downstream for the coated configurations. This trend is more evident for the 30 PPI case (Fig. 15(c)) than for the 10 PPI one (Fig. 15(e)). Indeed, the higher static permeability of the latter results in a more substantial flow penetration within the porous medium [47] that reduces the low-energy flow region in the near wake and limits the related increment in vortex-formation length. Such an effect is emphasised by the decrease in the equivalent cylinder diameter mentioned in Section 4.1. Similar conclusions on the link between the air-flow resistivity and the increase in vortex-formation length were also drawn by Sharma et al. [16].

Downstream of the recirculation zone, the periodic shedding of the vortical structures begins. This phenomenon can be observed from the mean-spanwise-vorticity contours: for the baseline (Fig. 15(b)), the regions of maximum and minimum Ω_z are spread over an area close to the cylinder surface, up to $x/d \approx 2$. When the 30 PPI coating is installed (Fig. 15(d)), the mean-spanwise-vorticity field features shear layers delimiting the wake that are initially thinner and more stable than the baseline, in agreement with Sueki et al. [12], and start expanding from $x/d \approx 4$, in correspondence with the recirculation zones. The transition between these two regions denotes the vortex-formation length. The same trend characterises the Ω_z contours for the 10 PPI case (Fig. 15(f)), although with a minor streamwise extent of the shear layers.

The vortex convection is visualised in the instantaneous-velocity-magnitude field in Fig. 5 for the 30 PPI metal-foam case together with the corresponding Γ_1 and Γ_2 contours in Fig. 16. At this time instant, a vortical structure characterised by a negative Γ_2 sign detaches from the shear layer at $x/d \approx 4.5$ and is convected by the mean flow. In such a process, the vorticity is subjected to sudden acceleration and deformation as it leaves the cylinder influence. The interaction of two counter-rotating eddies as they encounter together after the vortex-formation length may be connected with the dominant physical quadrupolar noise source discussed in Section 2 [7]. Two additional vortices with a positive sign are located upstream and downstream of this position. The former is still concentrated within the shear layer, whereas the latter is completely detached and lies at approximately 2 diameters of distance from the eddy with a negative Γ_2 sign.

The physical mechanism behind this increment in vortex-formation length is most likely associated with the presence of a slip velocity at the interface between the fluid and the porous medium [17]. The reduced velocity gradients on the surface of the coated cylinder weaken the shear layers and delay the roll-up of vortical structures [19]. At the same time, the flow re-injection from the leeward side of the cover induces entrainment layers that fill the potential suction region and increase the base pressure of the body [13], further contributing to the elongation of the vortex-formation length. This stabilisation effect may also be linked to a higher spanwise coherence possessed by the turbulent flow in the near-wake region, as previously observed by Geyer [15].

In addition, the porous coating has a strong effect on the distribution of the Reynolds stresses in the wake, in agreement with the literature results reviewed in Section 1. The study of the different components of the stress tensor is instrumental in quantifying the strength of the quadrupolar sound sources produced as a result of unsteady convection of flow, which is explicated by Eq. (8). Indeed,

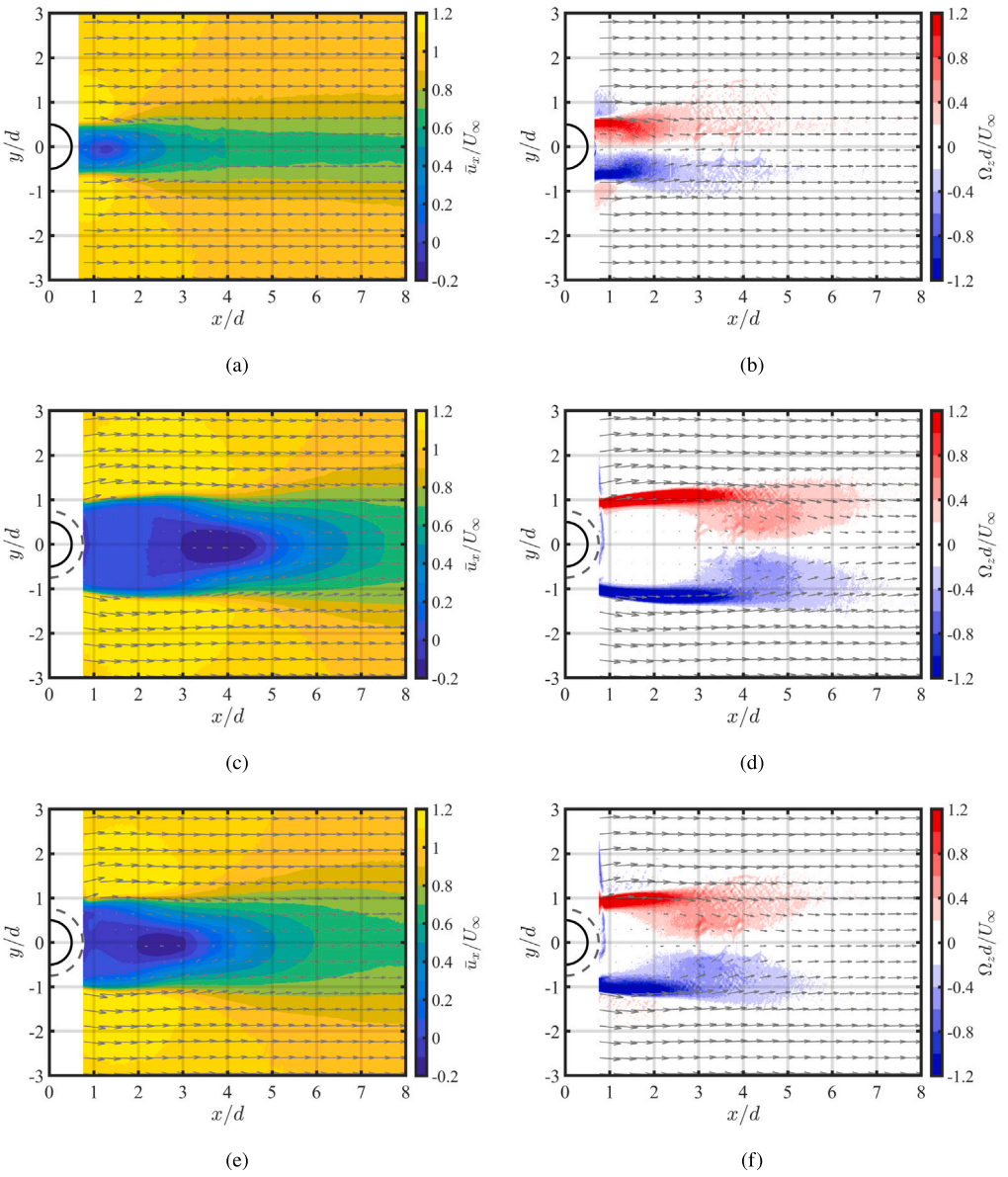

Fig. 15. Normalised flow statistics for the (a, b) bare cylinder and the cylinders coated with the (c, d) 30 PPI and (e, f) 10 PPI metal foams measured at $Re_d = 6.8 \times 10^4$: (a, c, e) mean streamwise velocity; (b, d, f) mean spanwise vorticity. The mean-flow streamlines are also indicated in the plot.

for high Reynolds numbers, the contribution of the viscous forces can be neglected and, with the assumption of incompressible and isentropic flow, Lighthill's stress tensor can be approximated as $T_{ij} \approx \rho u_i u_j$ [3].

Overall, the porous treatment of the circular cylinder has the two-fold effect of reducing the peak amplitude of the Reynolds stresses, spreading them out over a significantly wider area due to the larger equivalent diameter, and moving the region where turbulence is generated further downstream. Similarly to the previous observations, these trends are more pronounced for the 30 PPI coating than for the 10 PPI one. In particular, the streamwise Reynolds stresses τ'_{uu} (Figs. 17(a), 17(c) and 17(e)) are the most affected by porous cover. These components of the stress tensor are related to the flow recirculation and are greatly attenuated when the recirculation zone is shifted farther from the surface. On the other hand, the crosswise Reynolds stresses τ'_{vv} (Figs. 17(b), 17(d) and 17(f)) are associated with the oscillatory movement of the turbulent structures and are maximum at the location when the vortex shedding begins. Likewise, their peaks are substantially reduced by the porous treatment of the body. Analogous remarks can be made for the components τ'_{uv} of the Reynolds stress tensor (Figs. 18(a), 18(c) and 18(e)), even though their magnitude is considerably lower than that of the other components previously analysed.

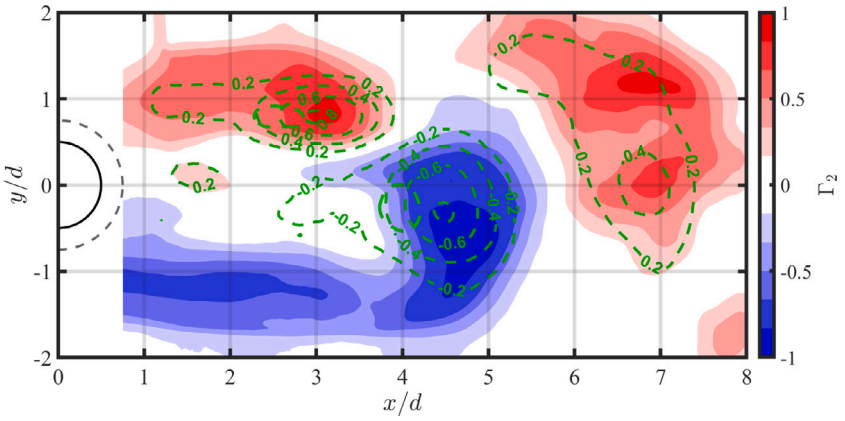

Fig. 16. Γ_2 function field for the cylinder coated with the 30 PPI metal foam at $Re_d = 6.8 \times 10^4$ corresponding to the instantaneous magnitude-velocity field in Fig. 5. The green dashed lines denote the values of the Γ_1 function.

In view of the above, the statistical flow parameter that most suitably represents the impact of the porous coating on the near-wake region is the turbulence kinetic energy k (Figs. 18(b), 18(d) and 18(f)), which is dominated by τ'_{vv} and is, therefore, maximum at the position where the vortex shedding is triggered. In this case, the reduction in the k peak amounts to approximately 45 % and 31 % for the 30 PPI and 10 PPI coatings, respectively. It is important to stress that, although the peak value of the turbulence kinetic energy is decreased, the larger area over which it extends likely results in an increase of its net integral value. These findings agree with those of Showkat Ali et al. [18].

4.3. Description of the noise-reduction mechanisms: focus on the quadrupole

The outcome of the aeroacoustic analysis in Fig. 6 shows that the cylinder coated with the least permeable cover is more effective in decreasing the tonal peak at the vortex-shedding frequency than the most permeable case. This finding is consistent with the fact that the flow behind the former configuration is more stable, and the onset of the shedding is located further downstream. The results confirm a link between the aerodynamic noise suppression due to the coating and the increase in vortex-formation length, which becomes more evident when the k contours are super-imposed on the beamforming sound-distribution maps. The comparisons between these two quantities at $f_{1/3} = 2.5\,\text{kHz}$ and $Re_d = 6.8 \times 10^4$ are shown in Figs. 19 and 20 for the baseline and the cylinder coated with the 30 PPI metal foam. All the values in the maps are expressed on a relative scale and normalised by the corresponding maxima. It is important to stress that the location of the downstream source shift is independent of the frequency, as demonstrated in Section 3.3. Hence, the findings discussed below are expected to be extendable to the whole part of the acoustic spectrum for which the noise induced by the turbulent-flow interaction within the pores does not dominate. For the baseline, the dominant noise sources are distributed over the cylinder trailing edge, i.e. slightly upstream of the peak region of the turbulence kinetic energy. In contrast, the dominant noise sources for the coated cylinder are located approximately in the area where the turbulent structures begin their oscillatory movement and the vorticity is subjected to rapid acceleration and deformation.

The findings discussed above suggest that approaching the problem from a sound-diffraction perspective can be instructive in the present case. A 2-D model of the sound scattered by the cylinder surface based on the works of Davies [48] and Gloerfelt et al. [9] is proposed here. Under the assumption of acoustic compactness, the noise-source region produced by the unsteady convection of flow at the vortex-shedding frequency can be represented as a point lateral quadrupole located at the position of maximum k. This equivalent source ensures that the anti-symmetry of the von Kármán street is maintained and constitutes the most suitable choice to represent the shedding instability. The model, whose parameters and details on the numerical domain and integration methods are reported in Appendix A, relies on the consideration that T_{ij} in the cylinder periodic wake is characterised by a strong tonal component that dominates the turbulence kinetic energy. This scenario is supported by the analysis of the spectrum of the upwash-velocity fluctuations downstream of the body, which features a prominent peak in correspondence with the vortex-shedding frequency, as illustrated in previous investigations [45,49]. In addition, the 2-D approach pursued in the study implicitly assumes that the calculated acoustic field is characterised by an infinite spanwise correlation length. In reality, this quantity can be estimated in the order of a few cylinder diameters for a fully developed 3-D wake [50], implying that every correlated element of the turbulent flow in the vicinity of the body can be considered acoustically compact at f_{VS} [9]. Such a hypothesis also applies to the coated configurations, despite the possible increase in spanwise correlation length induced by the porous cover [15]. Therefore, the conclusions that will be drawn below are not deemed to be affected by 3-D effects.

The circular cylinders are modelled as solid, perfectly reflecting surfaces whose dimensions are determined by their equivalent diameters, i.e. $d = 0.02\,\text{m}$, $d = 0.0308\,\text{m}$, and $d = 0.0285\,\text{m}$ for the baseline and the 30 PPI and 10 PPI coated configurations, respectively (see Section 4.1). For the last two, this choice is motivated by the consideration that the acoustic wavelength at the vortex-shedding frequency λ_{VS} is much larger than the average pore size of the permeable coatings d_p. For instance, $\lambda_{\text{VS}}/d_p \approx 1.29 \times 10^3$ and

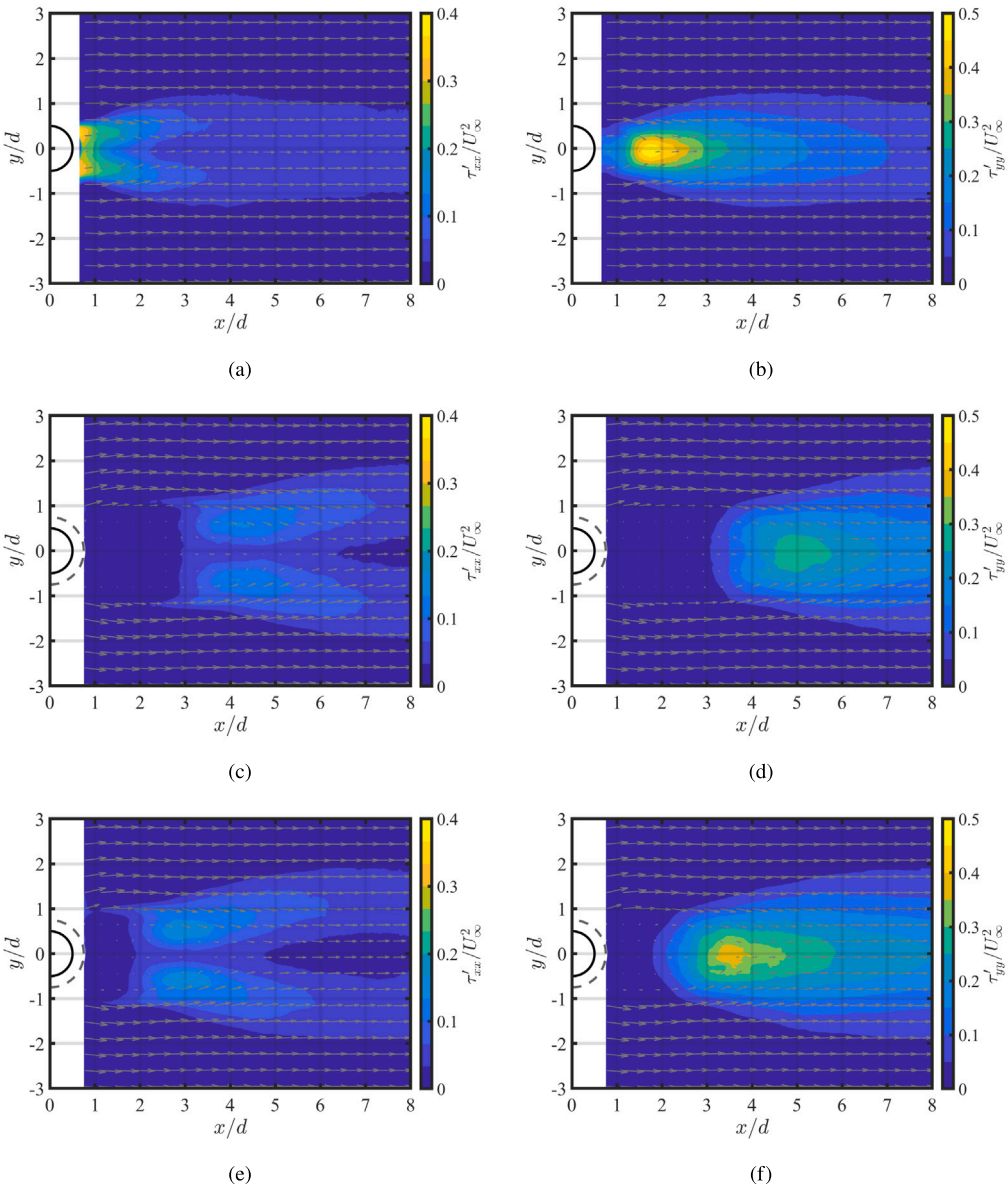

Fig. 17. Normalised flow statistics for the (a, b) bare cylinder and the cylinders coated with the (c, d) 30 PPI and (e, f) 10 PPI metal foams measured at $Re_d = 6.8 \times 10^4$: (a, c, e) component τ'_{xx} of the Reynolds stress tensor; (b, d, f) component τ'_{yy} of the Reynolds stress tensor. The mean-flow streamlines are also indicated in the plot.

$\lambda_{VS}/d_p \approx 4.05 \times 10^2$ for the 30 PPI and the 10 PPI metal foam, respectively. Noise sources that are potentially produced by a non-zero Reynolds stress at the surface [51] are not accounted for in the present formulation.

Regarding the determination of the quadrupole amplitude A, the lack of a time-resolved PIV dataset prevents $\hat{T}_{ij}$ from being directly evaluated at the vortex-shedding frequency. A different approach capable of linking the strength of the quadrupolar source associated with the periodic interaction of counter-rotating vortices, whose contribution is expected to dominate the turbulence-kinetic-energy field, with the time-averaged data extracted in the wake is thus required. Under the assumptions of acoustic compactness and geometric far field, the former being verified at f_{VS}, the volume sources of Lighthill's analogy in the time domain are dictated by the integral of the second derivative of T_{ij} with respect to time [52]. Such temporal dependency is also a function of the frequency at which the vortices are shed, which is, in turn, related to the equivalent diameter of the cylinder. This consideration can be exploited to determine an approximated value of A that, for each configuration, reflects the changes in the time variation of the turbulence quantities integrated over the whole fluid volume. The procedure is explained in detail in Appendix B. The resulting sound field is then computed using Eq. (8) and propagated in time, assuming a medium at rest. This simplified model tackles the

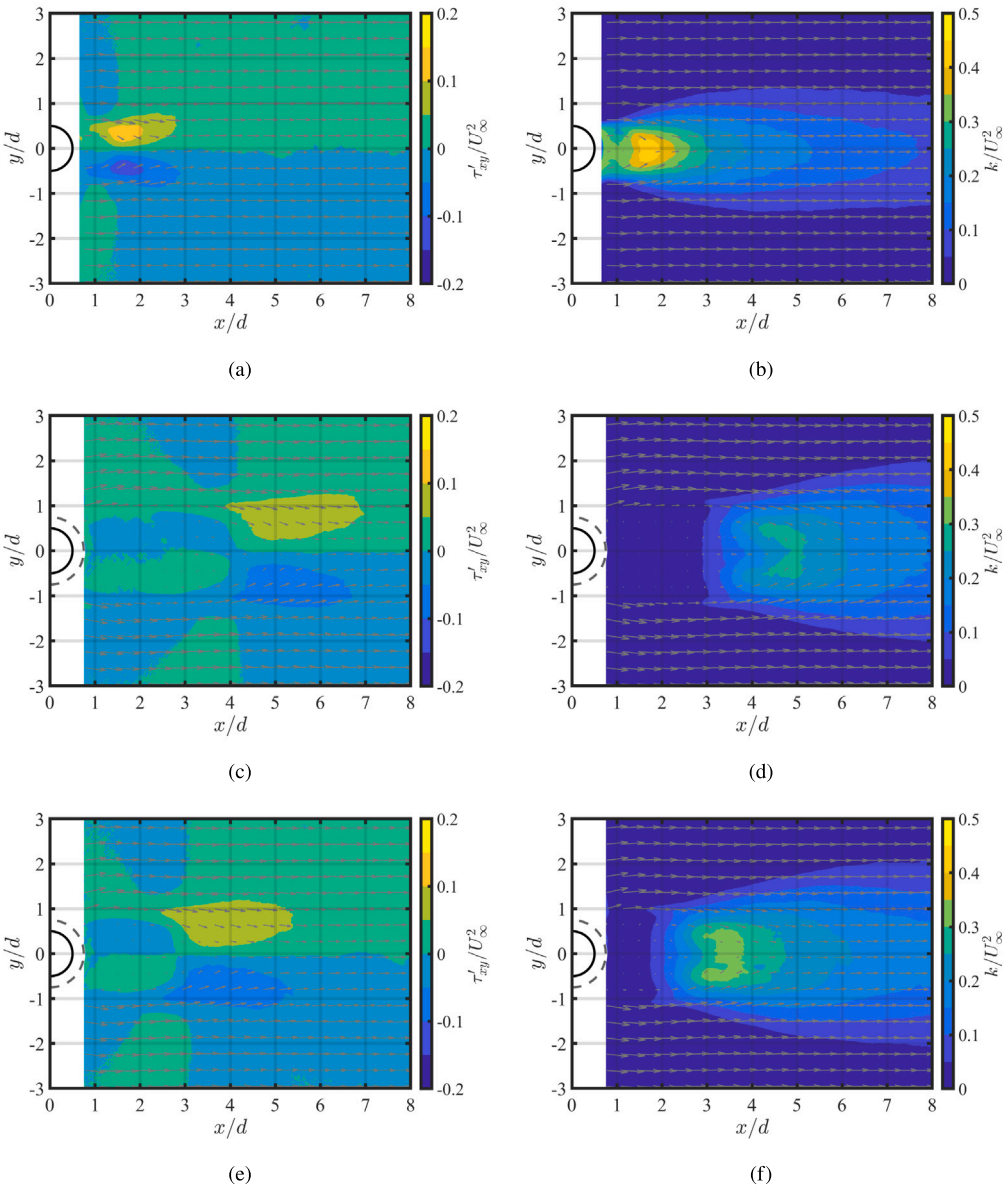

Fig. 18. Normalised flow statistics for the (a, b) bare cylinder and the cylinders coated with the (c, d) 30 PPI and (e, f) 10 PPI metal foams measured at $Re_d = 6.8 \times 10^4$: (a, c, e) component τ'_{xy} of the Reynolds stress tensor; (b, d, f) turbulence kinetic energy. The mean-flow streamlines are also indicated in the plot.

problem of the noise generated by the flow past a cylinder from a purely acoustic point of view. Indeed, outside of the near-wake region, the acoustic pressure fluctuations are the only sound-source components that propagate into the far field, differently from their hydrodynamic counterparts, which decay significantly with increasing distances from the surface [53].

The contributions to the acoustic-pressure field coming from the direct and scattered components of the tailored Green's function can now be analysed separately. In Fig. 21, snapshots of the direct and scattered fields, denoted as p'_d and p'_s, respectively, are shown for the baseline and the cylinder coated with the 30 PPI metal foam. The location of the central microphone of the array is also indicated in the figure. The results refer to $Re_d = 6.8 \times 10^4$, which corresponds to $f_{\mathrm{VS}} = 482.5$ Hz and $f_{\mathrm{VS}} = 308.3$ Hz for the bare and coated cylinders, respectively. Overall, p'_d exhibits the typical directivity pattern of a lateral quadrupole in the free field, whereas p'_s resembles that of a dipolar source whose axis is normal to the streamwise direction and whose origin is in the body, precisely at $x = d^2/(4\,L_q)$, as a consequence of the circle theorem [54]. Here, L_q denotes the distance of the quadrupole from the cylinder centre. For the baseline, the amplitude of the scattered acoustic field (Fig. 21(b)) is more significant than that of the direct acoustic field (Fig. 21(a)), supporting the assumption commonly made in Curle's analogy that quadrupolar compact sources are negligible

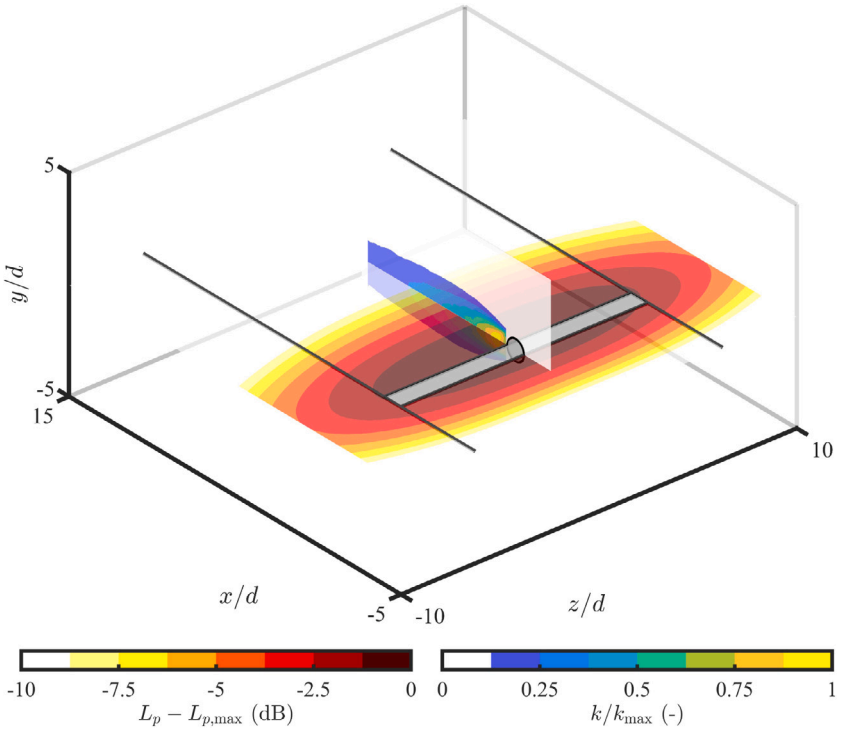

Fig. 19. Source-distribution map at $f_{1/3} = 2.5\,\mathrm{kHz}$ and turbulence kinetic energy contour for the bare cylinder at $Re_d = 6.8 \times 10^4$. The maps are normalised by the corresponding maximum values.

with respect to the dipolar ones in low Mach-number applications. In contrast, for the coated configuration, the two sound sources provide comparable contributions (Figs. 21(c) and 21(d)). The lower scattered radiation is, therefore, an implication of the increased distance between the source and the surface but also the decreased strength of the quadrupole, which, in turn, results in a weaker p'_d throughout the domain. Indeed, the outcome of the analysis in Appendix B demonstrates that, if the porous treatment of the cylinder does effectively not reduce the net integrated amplitude of Lighthill's stress tensor, it does, however, diminish its time derivative, decreasing, as a consequence, the radiation efficiency of the quadrupolar source.

The alterations in the relative weight of p'_d and p'_s at the vortex-shedding frequency visible in Fig. 21 affect the trend of the total acoustic pressure $p' = p'_d + p'_s$, which is illustrated in the snapshots in Fig. 22 for the bare and coated cylinders at $Re_d = 6.8 \times 10^4$. While the contribution of the scattered component mostly dominates the total acoustic field for the baseline (Fig. 22(a)), the coated configuration (Fig. 22(b)) features a quadrupolar source radiating from the cylinder wake into the far field with a quasi-dipolar directivity. Part of the scattered sound waves close to the body surface destructively interferes with the direct ones due to the boundary condition imposed by the tailored Green's function. This partial interference sets the origin of the noise source related to the total acoustic pressure in the cylinder wake, in correspondence with the compact-quadrupole position. From a physical perspective, such a scenario is consistent with the statement of Powell [4], who argued that the origin of the acoustic energy necessarily comes from the unsteady flow and cannot be generated on the cylinder surface. Moreover, although the computations refer to specific narrow frequencies, the proposed diffraction mechanism is likely extendable to the broadband range.

A more quantitative picture of the relative contributions of the direct and scattered acoustic fields to the total one for the baseline and the coated cylinder can be imparted by computing the time signals of the acoustic pressure evaluated at the location of the central microphone of the array and the associated directivity patterns, which are depicted in Figs. 23 and 24, respectively. For the latter, $p'_d(t)$ and $p'_s(t)$ are extracted at a distance of $r = 50\,d$, i.e. where the central microphone lies, and their standard deviations are computed over a total period of 10 vortex-shedding cycles to retrieve the sound pressure level. The overall predominance of the scattered field over the direct one is confirmed for the bare cylinder (Figs. 23(a) and 24(a)). p'_d yields a significant contribution to the total acoustic pressure only for directivity angles in the vicinity of the stagnation streamline, whereas it is negligible for $\pi/3 < \Theta < 2\pi/3$ and $4\pi/3 < \Theta < 5\pi/3$. The trend differs for the coated configuration (Figs. 23(b) and 24(b)), for which the direct acoustic field overcomes the scattered one for most angles except in the direction normal to the free stream, where the radiation efficiency of p'_s is maximum and that of p'_d is minimum. The fact that, at $\Theta = \pi/2$, the total acoustic pressure is predominately dominated by the scattered field, which is dipolar in nature, explains why the L_p spectra for the coated cylinders in Fig. 8 do not scale with the eight power of the Mach number, which would typically be linked to a quadrupolar source. It follows that the weaker the scattered field is, the narrower the observation-angle range surrounding $\Theta = \pm\pi/2$ for which a pseudo-dipolar sound directivity

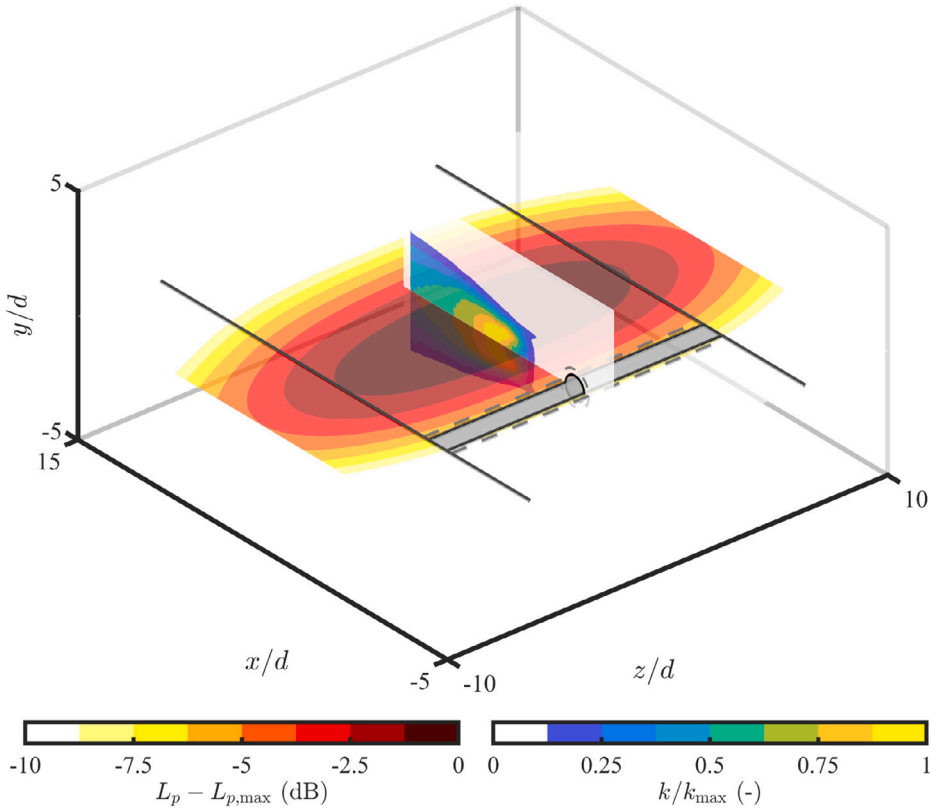

Fig. 20. Source-distribution map at $f_{1/3} = 2.5\,\text{kHz}$ and turbulence kinetic energy contour for the cylinder coated with the 30 PPI metal foam at $Re_d = 6.8 \times 10^4$. The maps are normalised by the corresponding maximum values.

will be. This is confirmed by the fact that the scaling factor of the spectra related to the coated cylinders is closer to that for a quadrupole at the most downstream microphone, corresponding to $\Theta \approx \pi/4$ (Fig. 9).

The framework outlined so far is now applied to elucidate the experimental results of the beamforming application in Section 4.1. This explanation builds on the following remarks. (i) Since the phased-array method is based on the free-field Green's function (see Section 3.3), both physical and image sources are theoretically present in the sound maps. The former are the quadrupoles in the wake radiating the direct acoustic field, whereas the latter are a consequence of the diffraction by the cylinder surface and constitute the origin of p'_s. However, their amplitudes depend on the relative contribution of the direct and scattered acoustic fields in the far field, which determines whether the sources lie within the same dynamic range in the sound map. (ii) As shown in Appendix C, the efficiency of the scattering mechanism, and thus the strength of the image source, decreases considerably with increasing vortex-formation length and frequency due to non-compactness effects. (iii) According to the aforementioned circle theorem [54], the location of the image source depends on the position of the physical one: the shorter L_q is, the closer the sources will be. At low frequencies, even if the two sources lie within the same dynamic range, the spatial resolution of the sound map may be too low to properly separate their noise contributions (see Eq. (15)). In this case, only one source distribution encompassing the origin for both direct and scattered acoustic fields will be displayed.

In view of the above, at low frequencies, the dominant source region for the bare cylinder most likely includes just the image source, explaining why the $L_{p(1/3)}$ peak appears to be located in the aft part of the body in Figs. 10(a) and 14(a). This hypothesis is supported by the directivity pattern in Fig. 24(a), which demonstrates that the sound recorded by the microphones of the array is dominated by the scattered field. At higher frequencies, the efficiency of the diffraction mechanism decreases, and the maps display the quadrupole as well as the image source as a unique noise source distributed over the cylinder's trailing edge (Fig. 11(a)). When the frequency further increases, the image source becomes weaker, and only the physical one in the near wake is visible (Figs. 12(a) and 13(a)).

For the coated cylinders, the image source in the broadband frequency range generally lies below the dynamic range of the sound map due to the larger vortex-formation length. This is the reason why just the quadrupolar source in the wake is found in Figs. 10(b), 10(c), 11(b), 11(c), 12(b) and 12(c) for the cylinder coated with the 30 PPI and 10 PPI coating, respectively. The scenario differs slightly at the vortex-shedding frequency. Indeed, the contribution of the image source appears to be also present in the sound map computed for f_{VS}, leading to the more pronounced streamwise extension of the dominant source distributions in Figs. 10(b) and 10(c), especially for the most permeable cover. This observation is consistent with the scaling analyses in Figs. 8 and 9, which

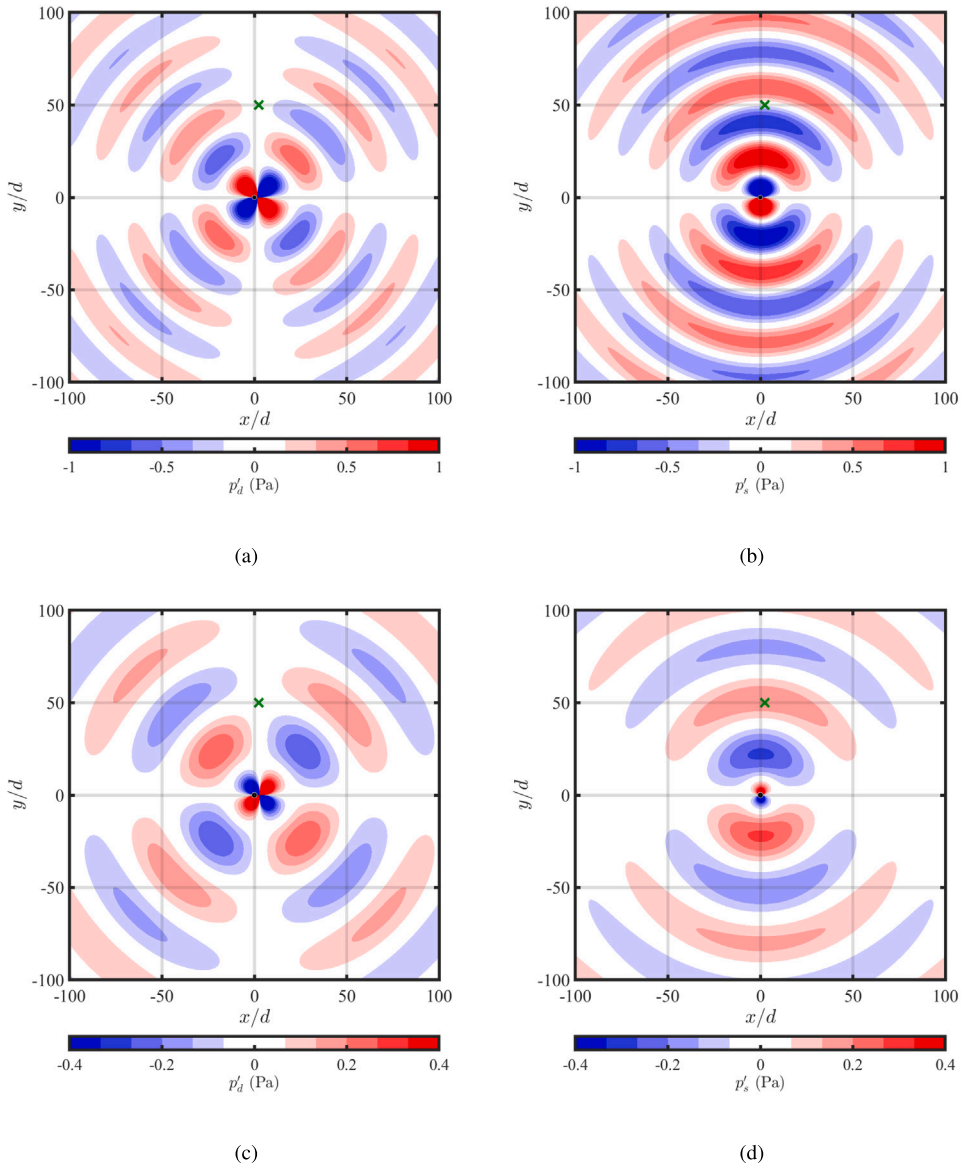

Fig. 21. Snapshots of (a, c) the acoustic pressure p'_d radiated by the single lateral quadrupolar source and (b, d) the acoustic pressure p'_s scattered by the cylinder surface at the vortex-shedding frequency for (a, b) the baseline and (c, d) the cylinder coated with the 30 PPI metal foam at $Re_d = 6.8 \times 10^4$. The green x symbols indicate the position of the central microphone of the array. The flow goes from the left to the right of the map.

prove that the tonal component of the frequency spectrum is closer to a dipolar directivity than the broadband one. It is important to stress that these results could not have been elucidated with the standard approach of Curle's analogy, where volume terms are neglected owing to the low Mach number.

The present methodology can be validated by comparing the peak-to-peak noise reduction predicted by the model with the experimental results. The standard deviation of the calculated time signal over 10 vortex-shedding cycles is evaluated at the position of the central microphone of the array (Fig. 23). The experimental and predicted ΔL_p, intended as the deviations of the levels produced by the coated cylinders from those radiated by the baseline, are visible in Fig. 25 for the two metal foams and different inflow velocities. For each configuration, the relative amplitudes of the point quadrupole and the vortex-formation lengths are determined from the PIV velocity-field contours. In general, a satisfactory agreement within 2 dB is found between experiments and calculations, independently of the free-stream velocity and the properties of the porous cover. Nevertheless, the prediction appears to consistently under-predict the noise attenuation, partially due to how the porous-fluid interface is treated in the model. Indeed, the outer metal-foam wall is assumed to be a perfectly reflecting surface at which $\partial p/\partial n = 0$. Imposing an impedance boundary condition based on the static permeability of the material would result in a more accurate representation of the acoustic field and possibly

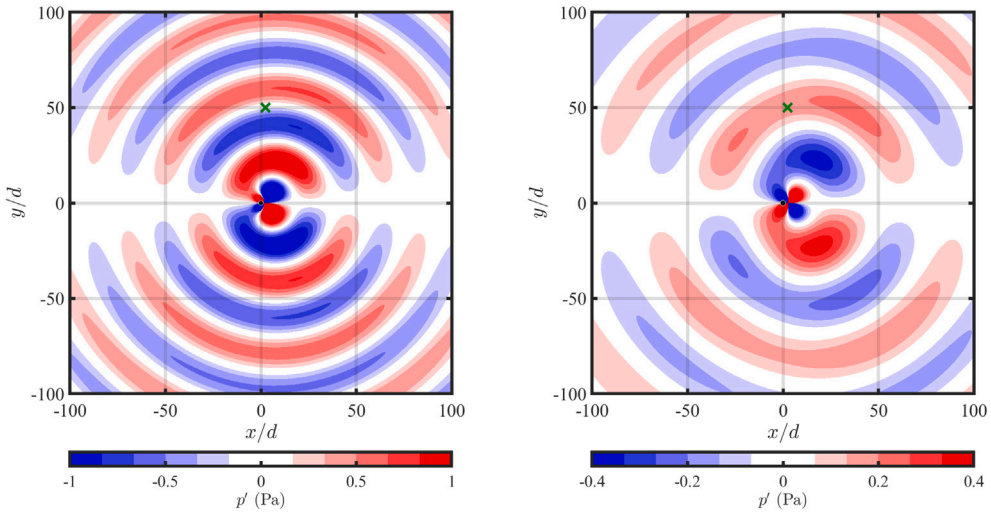

(a) (b)

Fig. 22. Snapshots of the total acoustic pressure $p' = p'_d + p'_s$ radiated at the vortex-shedding frequency by (a) the baseline and (b) the cylinder coated with the 30 PPI metal foam at $Re_d = 6.8 \times 10^4$. The green x symbols indicate the position of the central microphone of the array. The flow goes from the left to the right of the map.

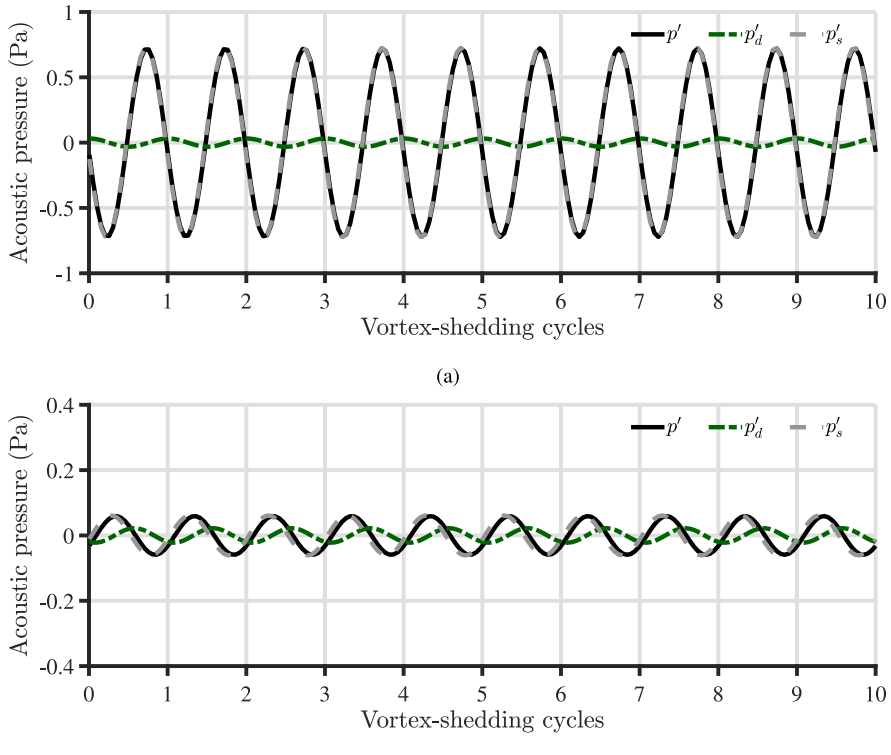

Fig. 23. Time series of the total, direct, and scattered acoustic pressure radiated at the vortex-shedding frequency by (a) the baseline and (b) the cylinder coated with the 30 PPI metal foam at $Re_d = 6.8 \times 10^4$ at the location of the central microphone of the array.

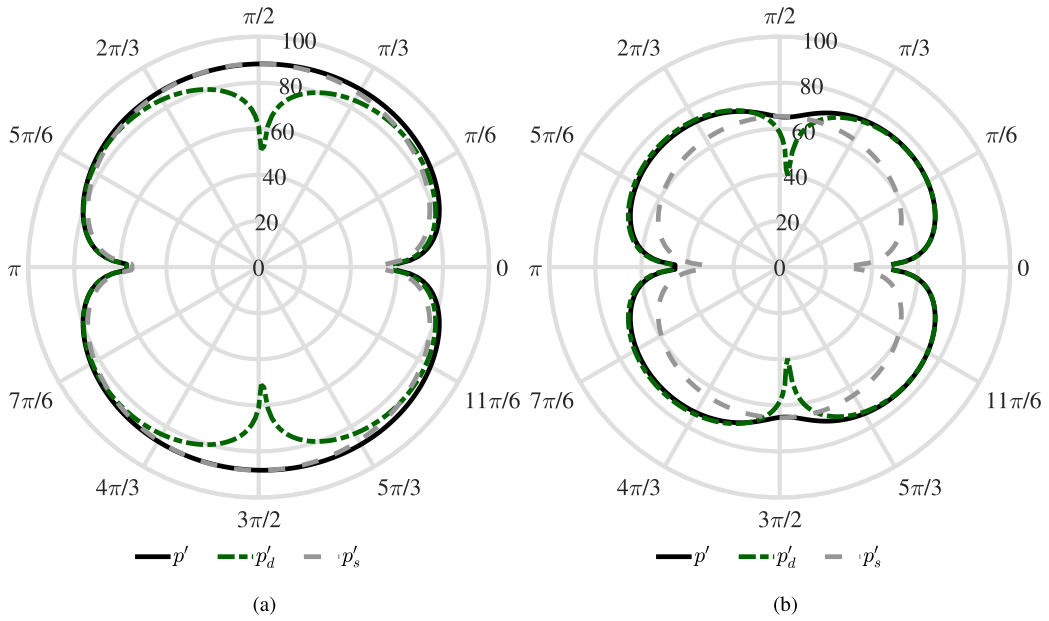

Fig. 24. Directivity patterns of the total, direct, and scattered acoustic pressure radiated at the vortex-shedding frequency by (a) the baseline and (b) the cylinder coated with the 30 PPI metal foam at $Re_d = 6.8 \times 10^4$ at a distance of $r = 50\,d$. The L_p values are expressed in dB with $p_{\text{ref}} = 20$ μPa.

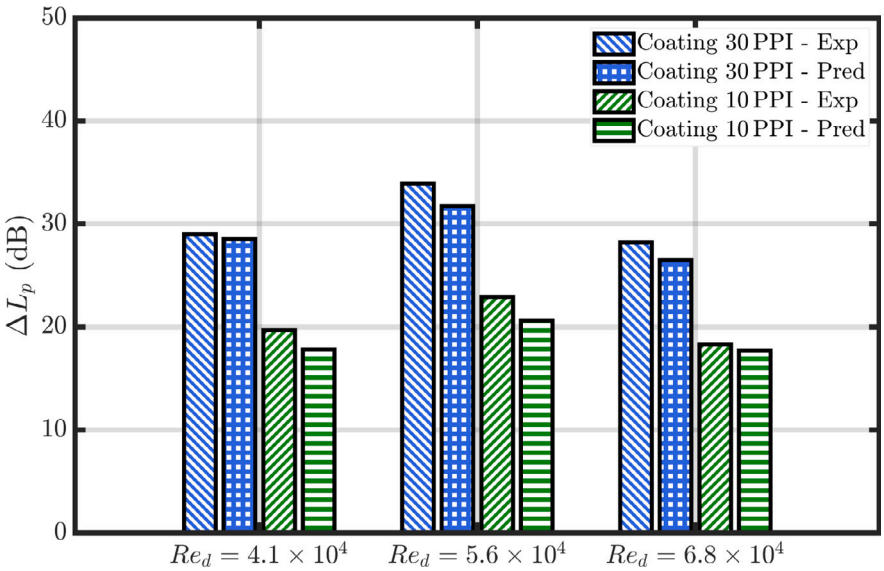

Fig. 25. Experimental and predicted peak-to-peak noise reduction at the vortex-shedding frequency for the cylinders coated with the 30 PPI and 10 PPI metal foams and different inflow velocities.

weaken the sound scattered by the coated cylinder, increasing the sound suppression. However, the relatively small deviation of the calculations from the measurements suggests that the contribution of the non-reflective surface to the noise mitigation at the vortex-shedding frequency is only secondary, supporting the use of the tailored Green's function in Eq. (11) also for the coated configurations. At higher frequencies, the pores of the permeable coating can no longer be deemed acoustically compact, and this assumption is expected to lose its validity.

These analytical results eventually enlighten the main noise-reduction mechanisms of the porous coating of a circular cylinder. The cover has a two-fold effect: on the one hand, it decreases the strength of the quadrupolar sources generated in the wake of the body at the position of the onset of the vortex shedding; on the other hand, it moves this location further downstream, reducing the efficiency of the sound scattered by the cylinder. As the outcome of the parametric study carried out in Appendix C illustrates, the latter mechanism has the most striking impact on the noise attenuation if the source displacement occurs in the near-wake

region. When the quadrupole is located farther than approximately 3 diameters from the surface, the scattered acoustic-pressure field becomes negligible compared with the direct one, and the sound mitigation is affected only by the decrease in source strength, which is linked to the attenuated temporal variation of the turbulence quantities in the wake.

In summary, the porous cover reduces aerodynamic noise by altering the way this noise is produced and affecting the relative contribution of dipoles and quadrupoles. As a consequence, the volume sources must be accounted for in the numerical modelling of the problem, even at low Mach numbers. This key result can elucidate why a permeable formulation of the acoustic analogy of Ffowcs Williams and Hawkings [55] proved to be more accurate than a solid one for simulations conducted on coated cylinders [56]. Interestingly, a similar conclusion was also reached in a numerical study by Turner and Kim [57] for low-speed flows past an aerofoil at high incidence angles. In particular, the quadrupole contribution was deemed far from negligible in the case of aerofoil stall.

Nonetheless, this approach cannot directly clarify the reason why the amplitudes of the dominant sources for the 30 PPI and 10 PPI cases are comparable in the broadband frequency range, as seen in the acoustic spectra and beamforming sound maps. A potential explanation relies upon a varying source strength characterising the lateral quadrupole at frequencies different from f_{VS}. The integration of Lighthill's stress tensor according to Eq. (8) could shed light on this trend, making it possible to quantify the amplitude of the quadrupolar sources throughout the spectrum and their diffraction by the body. Non-compact and 3-D effects arising at higher frequencies would be additionally accounted for in this way, as well as possible uncertainties associated with the positioning and relative strength of the point source representing the origin of the acoustic energy.

5. Conclusions

The present research clarifies the link between the near-wake characteristics downstream of a circular cylinder coated with a porous material and the corresponding aerodynamic noise reduction. This objective has been pursued by combining, for the first time, sound-localisation and flow-visualisation techniques with analytical modelling. The experimental results show that, for a coated cylinder, the dominant noise sources lie in the flow, in a region downstream of the body that is determined by the vortex-formation length, whereas far-field noise features a quasi-dipolar directivity pattern. This finding does not agree with the common view associated with Curle's analogy, according to which the sound is produced by the fluctuating force that the cylinder exerts on the surrounding fluid and the volume terms in the wake can be neglected. It can rather be elucidated by formulating the flow-induced noise of a bluff body as a diffraction problem by means of a tailored Green's function. Indeed, the results of the analytical model reveal that the Aeolian tone is generated by a compact quadrupolar source located at the vortex-shedding onset position that is scattered by the surface, radiating sound into the far field as a dipole. The acoustic energy comes thus from the unsteady flow itself. The presence of a coating on the cylinder lowers its strength amplitude by decreasing the temporal variation of the turbulence quantities in the wake and moves its origin further downstream, reducing the efficiency of the diffraction mechanism. In particular, the impact of the scattering can be deemed negligible for displacements of the quadrupole more than 3 diameters downstream of the body. Notably, the impedance boundary condition that characterises the porous interface plays a secondary role in noise mitigation. Therefore, the flow-permeable cover directly affects the aerodynamic sound generation and alters the relative weight of the equivalent acoustic sources at stake. The interpretation of the flow-induced cylinder noise and its consequent attenuation due to the porous coatings proposed in this study is the only one that can explain the experimental findings of the measurement campaign.

The physics outlined above has relevant implications for the numerical modelling of flow instabilities in the vicinity of scattering surfaces. Specifically, the analysis has indicated that an instability developing in the flow field leads to a quadrupolar source that cannot be neglected for the correct prediction of the noise radiated by a coated cylinder. Its effect has been assessed to provide a contribution similar to that of the surface dipoles, which could not be revealed without using a tailored Green's function. Besides indicating that appropriate precautions should be taken into account for these quadrupolar sources in the computation of the far-field noise, which may also require a compressible numerical solver, this research raises the question about the aeroacoustic modelling of inherent instabilities in the flow. The generation of a simulated data set would make it possible to extend the present analysis by directly integrating the different components of Lighthill's stress tensor and will be a topic for future work. In this perspective, the extensive experimental database produced in the study can serve as support for the validation of numerical computations.

Finally, the outcome of this research not only improves the understanding of the noise-reduction mechanisms of a porous coating of the cylinder but also provides guidelines for a more effective design of passive sound-control strategies. Maximising the downstream source shift represents a valid design criterion for the treatment of a bluff body, which could be achieved with an optimisation of the porous medium within the cover, exploiting the recent advancements in additive manufacturing techniques, or a modification of the body shape. Indeed, the presence of a uniform coating around the cylinder is potentially not indispensable for producing the same effect, opening up new disruptive paths for integrating these technologies into industrial applications. A successful example of this application has been recently proposed by the authors [23]. Nonetheless, eventual shape alterations could additionally lead to changes in the noise-diffraction mechanisms, and caution should be exercised when designing technological solutions based on this criterion to avoid potential amplification of the sound scattered by the body.

CRediT authorship contribution statement

R. Zamponi: Writing – original draft, Visualization, Validation, Software, Methodology, Investigation, Formal analysis, Data curation, Conceptualization. **F. Avallone:** Writing – review & editing, Supervision, Methodology, Investigation. **D. Ragni:** Writing – review & editing, Supervision, Project administration, Funding acquisition, Data curation. **C. Schram:** Writing – review & editing, Supervision, Methodology, Formal analysis. **S. van der Zwaag:** Writing – review & editing, Supervision, Project administration, Funding acquisition.

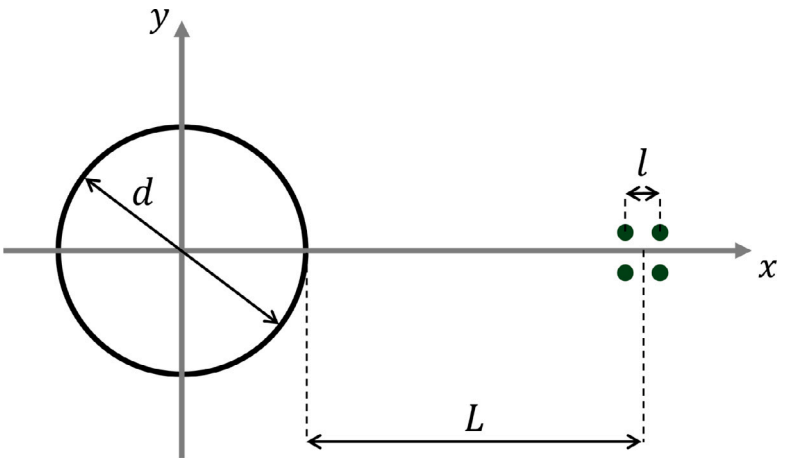

Fig. A.1. Notations used for the definition of the lateral quadrupole source.
Source: Picture adapted from Gloerfelt et al. [9]

Data availability

Data will be made available on request.

Acknowledgements

This research is part of the IPER-MAN project (Innovative PERmeable Materials for Airfoil Noise Reduction), project number 15452, funded by The Dutch Research Council (NWO). The authors gratefully acknowledge Prof. M. Roger from École Centrale de Lyon for the fruitful discussions on the work.

Declaration of competing interest

The authors declare that they have no known competing financial interests or personal relationships that could have appeared to influence the work reported in this paper.

Appendix A. Modelling of sound scattering by a cylinder

The lateral quadrupole in the analytical model proposed in Section 4.3 can be constructed by adding four point sources having the same strength and opposite signs. With respect to Fig. A.1, the positive sources are located at $(x, y) = (d/2 + L + l/2, l/2)$ and $(x, y) = (d/2 + L - l/2, -l/2)$, whereas the negative ones at $(x, y) = (d/2 + L - l/2, l/2)$ and $(x, y) = (d/2 + L + l/2, -l/2)$. Here, L and l are the distance between the body surface and the equivalent source centre and the separation distance between two point sources, respectively. A value of $l = 0.5\,\mathrm{mm}$ allows the quadrupole to be assumed compact at the considered frequencies, while L is determined for each case by the position where the turbulence kinetic energy is maximum.

Under these assumptions, the integration of Eq. (8) for a compact quadrupole placed at $\mathbf{y} = (r_y, 0)$ and an observer located at $\mathbf{x} = (r_x, \Theta_x)$ yields the following expressions for the direct and scattered acoustic-pressure fields [9]:

$$\hat{p}_d(\mathbf{x}, \omega) = \frac{A}{4\mathrm{i}} \left[-k_0^2 \frac{r_1 r_2}{r^2} H_0^{(1)}(k_0 r) + k_0 \frac{2 r_1 r_2}{r^3} H_1^{(1)}(k_0 r) \right], \tag{A.1}$$

where $r_1 = r_x \cos\Theta_x - r_y$, $r_2 = r_x \sin\Theta_x$, and $r = (r_1^2 + r_2^2)^{1/2}$, and

$$\hat{p}_s(\mathbf{x}, \omega) = \frac{A}{4\mathrm{i}} \sum_{m=0}^{+\infty} \epsilon_m m \sin(m\Theta_x) \frac{J_{m-1}(k_0 d/2) - J_{m+1}(k_0 d/2)}{H_{m-1}^{(1)}(k_0 d/2) - H_{m+1}^{(1)}(k_0 d/2)} H_m^{(1)}(k_0 r_x) \left[-\frac{1}{r_x^2} H_m^{(1)}(k_0 r_y) - \frac{k_0}{r_x} H_{m+1}^{(1)}(k_0 r_y) + \frac{m}{r_x^2} H_m^{(1)}(k_0 r_y) \right]. \tag{A.2}$$

The acoustic-pressure fields displayed in Figs. 21 and 22 have been computed using a polar mesh-grid that contains approximately 12 million points ranging from $r_x = d$ to $r_x = 200\,d$, whereas the summation in Eq. (A.2) has been performed with a maximum m of 20.

Table B.1
Relative percentages of the point-quadrupole amplitude A for the coated configurations with respect to the baseline.

U_∞ (m s^{-1})	30	40	50
30 PPI	0.4672	0.4564	0.4659
10 PPI	0.7037	0.6884	0.7040

Appendix B. Determination of the quadrupolar source strength

The procedure followed to determine the coefficient A in Eqs. (A.1) and (A.2) for the bare and coated cylinders is outlined in this section. Since only the relative sound pressure levels are of interest, the absolute strength of the point quadrupolar source for the baseline at the different inflow velocities is manually tuned to match the corresponding vortex-shedding tonal peak from the experiments, following Gloerfelt et al. [9]. For the coated configurations, this value is then scaled according to the rate of change of the integrated Lighthill's stress tensor over time occurring in the fluid region. As mentioned in Section 4.3, the passage from the frequency to the time domain is made necessary by the impossibility of evaluating the frequency content of T_{ij} from a non-time-resolved PIV dataset. A simplified way to assess such temporal dependency is proposed hereafter.

Considering that the velocity field in the body wake features a strong tonal component at f_{VS} due to the periodic oscillations of the shed vortices, it is reasonable to assume that, to a first approximation, the large structures that determine the $T_{ij} \approx \rho u_i u_j$ amplitude also have a predominant periodic component characterised by an angular frequency $\omega = 2\pi f_{VS}$. This assumption is supported by the experimental evidence of Geyer [15], who showed that the tonal vortex-shedding peak dominates the spectra of the turbulent velocity fluctuations in the flow past solid and porous cylinders made of different materials. In contrast, the broadband components feature significantly lower values and can be deemed negligible. Consequently, when the second derivative with respect to time is performed, a factor ω^2 that multiplies T_{ij} and can be moved outside of the integral sign appears.

For the different configurations, the compact-quadrupole amplitude is thereby a function of the integral of Lighthill's stress tensor over the volume, which is proportional to the integral of k, as well as the angular frequency associated with the vortex shedding. Given the definition of f_{VS}, the term that multiplies the volume integral is $(2\pi\, St_{VS}\, U_\infty/d)^2$ for the baseline and $(2\pi\, St_{VS}\, U_\infty/D_{eq})^2$ for the coated cylinders. From a physical perspective, the increase in outer diameter due to the porous cover reduces the frequency at which the shedding instability occurs, decreasing, in turn, the temporal variation of the turbulence quantities in the wake.

In light of the above, a possible method to estimate the relative source strength for each coated cylinder with respect to the bare one and at a prescribed free-stream velocity is to compute the integral of the turbulence kinetic energy over the fluid region, divide it by that of the baseline, and multiply it by a factor $(d/D_{eq})^2 < 1$. This quantity eventually provides the percentage by which the quadrupole absolute amplitude related to the bare cylinder needs to be scaled to retrieve the coefficients A for the two coated configurations. The corresponding results for the different flow speeds are summarised in Table B.1 and indicate that the source strength is actually attenuated by the porous treatment of the body, especially for the 30 PPI cover. This reduction represents the product of two counteracting effects: the increase in the net integral contribution of k due to the wider wake region, which was already highlighted in Section 4.2, and the decrease in f_{VS} caused by the larger equivalent diameter. The impact of the latter is more significant.

It is important to remember that the present method to estimate A provides just an approximation of the effective strength of the equivalent compact quadrupole radiating sound at the vortex-shedding frequency. A minor error caused by the partial truncation of the wake flow due to the limited field of view of the PIV is also foreseen in this case. Only the integration of Eq. (8) with time-resolved data would make it possible to quantitatively determine the true amplitude of the quadrupolar source. Nevertheless, as will be demonstrated by the analysis in Appendix C, the effect of the decreasing source strength is less significant than that of moving the quadrupole origin away from the scattering surface. Hence, possible inaccuracies in the computation of A are not expected to alter the conclusions drawn in this paper.

Appendix C. Relative influence of the noise-reduction mechanisms

The specific contributions of the two physical mechanisms described in Section 4.3 to the overall noise mitigation can be determined with a parametric study. The effects of the increasing distance of the compact quadrupole from the cylinder surface and reduction in its strength are analysed in Fig. C.1, which depicts the relative sound pressure levels measured at the central microphone location for the different vortex-shedding frequencies. The diameter of the body has been kept constant at $d = 0.02$ m, whereas the source amplitude is varied by multiplying the parameter A in Eqs. (A.1) and (A.2) by a factor that ranges from 0 to 1. The closer downstream position at which the quadrupole is evaluated corresponds to the vortex-formation length for the bare cylinder.

For every frequency, the L_p values steeply decrease with increasing displacement of the quadrupole up to $x/d \approx 3$, after which they start gradually increasing again. This trend can be explained by the relative weights of the direct and scattered components that vary in function of the distance from the surface. As observed in Fig. 21, p'_s dominates over p'_d close to the cylinder and gets monotonically more attenuated when moving away from it. At $x/d \approx 3$, its contribution is comparable to that of the direct acoustic-pressure field, which is, instead, not affected by the proximity to the body. This analysis agrees with the time series and directivity patterns shown in Figs. 23 and 24, respectively. For $x/d > 3.5$, p'_s becomes negligible. Besides, an increasing downstream

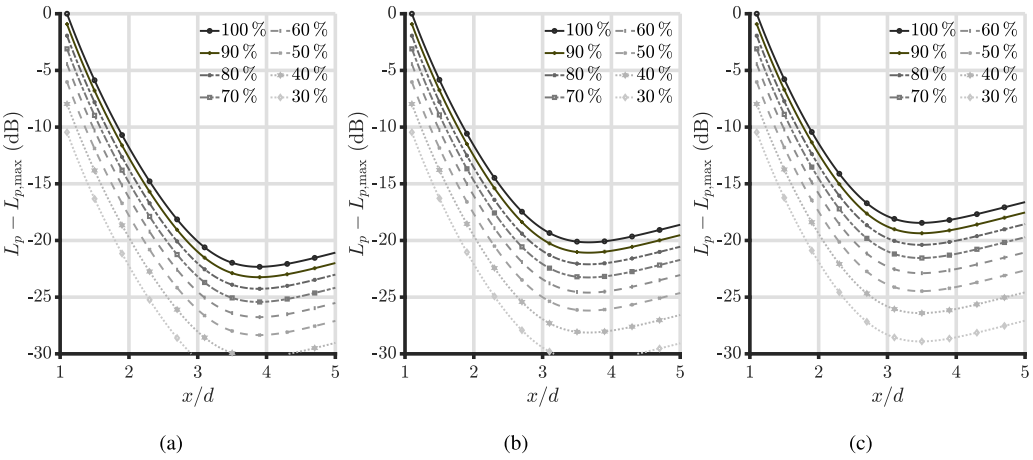

Fig. C.1. Relative difference in the total sound pressure level radiated by a circular cylinder to varying downstream shifts of the quadrupole source at (a) $f = 277.5\,\text{Hz}$, (b) $f = 370\,\text{Hz}$, and (c) $f = 462.5\,\text{Hz}$. The different curves refer to different percentages of the source amplitude A.

source shift produces a slight increment in the p'_d measured by the microphone due to the quadrupolar directivity of the radiated sound. Regarding the influence of the weakened source strength, reducing A results in a constant offset of the curves towards lower L_p values. The more significant the decrease is, the larger the offset becomes.

Finally, the effect of the two mechanisms on noise mitigation depends also on the frequency of interest. Particularly, greater overall reductions are achieved at minor f, for which the scattered field dominates more over the direct one. Indeed, the efficiency of the sound diffracted by the surface is higher when the noise-source regions represented by the cylinder and quadrupole are compact, i.e. $k\,L \ll 1$ [9]. The smaller the considered acoustic wave number is, the more valid this condition will be, affecting the values of $L_{p,\max}$ in Fig. C.1 and, particularly, the range of x/d for which $p'_s > p'_d$. Furthermore, the strength of the quadrupolar source radiating the direct field is reduced when f_{VS} decreases, as already demonstrated in Appendix B. As a consequence, the fact that the vortex shedding for a coated configuration occurs at lower frequencies than for the bare one at the same inflow velocity additionally contributes to the noise attenuation generated by the porous treatment.

References

[1] V. Strouhal, Ueber eine besondere Art der Tonerregung (on a special type of sound excitation), Ann. Phys. 241 (10) (1878) 216–251, http://dx.doi.org/10.1002/andp.18782411005.

[2] N. Curle, The influence of solid boundaries upon aerodynamic sound, Proc. Roy. Soc. Lond. A Mat. 231 (1187) (1955) 505–514, http://dx.doi.org/10.1098/rspa.1955.0191.

[3] M.J. Lighthill, On sound generated aerodynamically I. general theory, Proc. Roy. Soc. Lond. A Mat. 211 (1107) (1952) 564–587, http://dx.doi.org/10.1098/rspa.1952.0060.

[4] A. Powell, Theory of Vortex sound, J. Acoust. Soc. Am. 36 (1) (1964) 177–195, http://dx.doi.org/10.1121/1.1918931.

[5] J.E. Ffowcs Williams, L.H. Hall, Aerodynamic sound generation by turbulent flow in the vicinity of a scattering half plane, J. Fluid Mech. 40 (04) (1970) 657, http://dx.doi.org/10.1017/S0022112070000368.

[6] D.G. Crighton, F.A. Leppington, On the scattering of aerodynamic noise, J. Fluid Mech. 46 (3) (1971) 577–597, http://dx.doi.org/10.1017/S0022112071000715.

[7] M.S. Howe, Acoustics of Fluid-Structure Interactions, Cambridge University Press, 1998.

[8] R.D. Blevins, Review of sound induced by vortex shedding from cylinders, J. Sound Vib. 92 (4) (1984) 455–470, http://dx.doi.org/10.1016/0022-460X(84)90191-3.

[9] X. Gloerfelt, F. Pérot, C. Bailly, D. Juvé, Flow-induced cylinder noise formulated as a diffraction problem for low Mach numbers, J. Sound Vib. 287 (1–2) (2005) 129–151, http://dx.doi.org/10.1016/j.jsv.2004.10.047.

[10] V. Kopiev, I. Belyaev, M. Zaytsev, K. Zhao, Experimental study of truncated-cylinder struts for noise reduction of large-scale landing gears, J. Sound Vib. 511 (2021) 116362, http://dx.doi.org/10.1016/j.jsv.2021.116362.

[11] S. Rashidi, M. Hayatdavoodi, J.A. Esfahani, Vortex shedding suppression and wake control: A review, Ocean Eng. 126 (2016) 57–80, http://dx.doi.org/10.1016/j.oceaneng.2016.08.031.

[12] T. Sueki, T. Takaishi, M. Ikeda, N. Arai, Application of porous material to reduce aerodynamic sound from bluff bodies, Fluid Dyn. Res. 42 (1) (2010) 015004, http://dx.doi.org/10.1088/0169-5983/42/1/015004.

[13] H. Liu, J. Wei, Z. Qu, Prediction of aerodynamic noise reduction by using open-cell metal foam, J. Sound Vib. 331 (7) (2012) 1483–1497, http://dx.doi.org/10.1016/j.jsv.2011.11.016.

[14] T. Geyer, E. Sarradj, Circular cylinders with soft porous cover for flow noise reduction, Exp. Fluids 57 (3) (2016) 30, http://dx.doi.org/10.1007/s00348-016-2119-7.

[15] T. Geyer, Experimental evaluation of cylinder vortex shedding noise reduction using porous material, Exp. Fluids 61 (7) (2020) 153, http://dx.doi.org/10.1007/s00348-020-02972-0.

[16] S. Sharma, T. Geyer, E.J.G. Arcondoulis, On the influence of porous coating thickness and permeability on passive flow and noise control of cylinders, J. Sound Vib. 549 (2023) 117563, http://dx.doi.org/10.1016/j.jsv.2023.117563.

[17] H. Naito, K. Fukagata, Numerical simulation of flow around a circular cylinder having porous surface, Phys. Fluids 24 (11) (2012) 117102, http://dx.doi.org/10.1063/1.4767534.

[18] S.A. Showkat Ali, X. Liu, M. Azarpeyvand, Bluff body flow and noise control using porous media, in: 22nd AIAA/CEAS Aeroacoustics Conference, American Institute of Aeronautics and Astronautics, Lyon, France, 2016, http://dx.doi.org/10.2514/6.2016-2754.

[19] J. Aguiar, H. Yao, Y. Liu, Passive flow/noise control of a cylinder using metal foam, in: the 23rd International Congress on Sound and Vibration, The International Institute of Acoustics and Vibration, 2016, p. 9.

[20] C. Xia, Z. Wei, H. Yuan, Q. Li, Z. Yang, POD analysis of the wake behind a circular cylinder coated with porous media, J. Vis. 21 (6) (2018) 965–985, http://dx.doi.org/10.1007/s12650-018-0511-5.

[21] S. Sadeghipour, S.A. Showkat Ali, X. Liu, M. Azarpeyvand, G. Thorpe, Control of flows around bluff bodies mediated by porous materials, Exp. Therm. Fluid Sci. 114 (2020) 110048, http://dx.doi.org/10.1016/j.expthermflusci.2020.110048.

[22] Y. Sato, Y. Hattori, Mechanism of reduction of aeroacoustic sound by porous material: Comparative study of microscopic and macroscopic models, J. Fluid Mech. 929 (2021) A34, http://dx.doi.org/10.1017/jfm.2021.884.

[23] R. Zamponi, D. Ragni, S. Van Der Zwaag, F. Avallone, Innovative coatings for reducing flow-induced cylinder noise by altering the sound diffraction, Phys. Fluids 35 (12) (2023) 127120, http://dx.doi.org/10.1063/5.0177263.

[24] R. Zamponi, F. Avallone, D. Ragni, S. van der Zwaag, On the aerodynamic-noise sources in a circular cylinder coated with porous materials, in: 28th AIAA/CEAS Aeroacoustics 2022 Conference, American Institute of Aeronautics and Astronautics, Southampton, UK, 2022, http://dx.doi.org/10.2514/6.2022-3042.

[25] P.E. Doak, Acoustic radiation from a turbulent fluid containing foreign bodies, Proc. Roy. Soc. Lond. A Mat. 254 (1276) (1960) 129–146, http://dx.doi.org/10.1098/rspa.1960.0010.

[26] P.M. Morse, K.U. Ingard, Theoretical Acoustics, Princeton University Press, 1986.

[27] R. Merino-Martínez, A. Rubio Carpio, L.T. Lima Pereira, S. van Herk, F. Avallone, D. Ragni, M. Kotsonis, Aeroacoustic design and characterization of the 3D-printed, open-jet, anechoic wind tunnel of Delft university of technology, Appl. Acoust. 170 (2020) 107504, http://dx.doi.org/10.1016/j.apacoust.2020.107504.

[28] R. Porteous, D.J. Moreau, C. Doolan, A review of flow-induced noise from finite wall-mounted cylinders, J. Fluids. Struct. 51 (2014) 240–254, http://dx.doi.org/10.1016/j.jfluidstructs.2014.08.012.

[29] E.J.G. Arcondoulis, Y. Liu, Z. Li, Y. Yang, Y. Wang, Structured porous material design for passive flow and noise control of cylinders in uniform flow, Materials 12 (18) (2019) 2905, http://dx.doi.org/10.3390/ma12182905.

[30] A. Rubio Carpio, R. Merino Martínez, F. Avallone, D. Ragni, M. Snellen, S. van der Zwaag, Experimental characterization of the turbulent boundary layer over a porous trailing edge for noise abatement, J. Sound Vib. 443 (2019) 537–558, http://dx.doi.org/10.1016/j.jsv.2018.12.010.

[31] D.B. Ingham, I. Pop, Transport Phenomena in Porous Media, Elsevier, 1998, http://dx.doi.org/10.1016/B978-0-08-042843-7.X5000-4.

[32] E. Baril, A. Mostafid, L.P. Lefebvre, M. Medraj, Experimental demonstration of entrance/exit effects on the permeability measurements of porous materials, Adv. Eng. Mater. 10 (9) (2008) 889–894, http://dx.doi.org/10.1002/adem.200800142.

[33] N. Dukhan, K.P. Patel, Effect of sample's length on flow properties of open-cell metal foam and pressure-drop correlations, J. Porous Mater. 18 (6) (2011) 655–665, http://dx.doi.org/10.1007/s10934-010-9423-z.

[34] S. Luesutthiviboon, D. Ragni, F. Avallone, M. Snellen, An alternative permeable topology design space for trailing-edge noise attenuation, Int. J. Aeroacoust. 20 (3–4) (2021) 221–253, http://dx.doi.org/10.1177/1475472X211003295.

[35] L. Rayleigh, Investigations in optics, with special reference to the spectroscope, Lond. Edinb. Dubl. Phil. Mag 8 (49) (1879) 261–274.

[36] P. Welch, The use of fast Fourier transform for the estimation of power spectra: A method based on time averaging over short, modified periodograms, IEEE Trans. Audio Electroacoust. 15 (2) (1967) 70–73, http://dx.doi.org/10.1109/TAU.1967.1161901.

[37] A. Brandt, Noise and Vibration Analysis: Signal Analysis and Experimental Procedures, John Wiley & Sons, 2011.

[38] C.S. Allen, W.K. Blake, R.P. Dougherty, D. Lynch, P.T. Soderman, J.R. Underbrink, Aeroacoustic Measurements, Springer Berlin Heidelberg, 2002, http://dx.doi.org/10.1007/978-3-662-05058-3.

[39] R. Zamponi, Investigation of Turbulence-Surface Interaction Noise Mechanisms and Their Reduction Using Porous Materials (Ph.D. thesis), Delft University of Technology, 2021, http://dx.doi.org/10.4233/uuid:d332c7e3-87be-4ed6-aa71-e629ef77e07a.

[40] P. Sijtsma, Phased Array Beamforming Applied to Wind Tunnel And Fly-Over Tests, Technical Report, National Aerospace Laboratory, 2010.

[41] F. Scarano, M.L. Riethmuller, Advances in iterative multigrid PIV image processing, Exp. Fluids 29 (7) (2000) S051–S060, http://dx.doi.org/10.1007/s003480070007.

[42] B. Wieneke, PIV uncertainty quantification from correlation statistics, Meas. Sci. Technol. 26 (7) (2015) 074002, http://dx.doi.org/10.1088/0957-0233/26/7/074002.

[43] A. Sciacchitano, B. Wieneke, PIV uncertainty propagation, Meas. Sci. Technol. 27 (8) (2016) 084006, http://dx.doi.org/10.1088/0957-0233/27/8/084006.

[44] L. Graftieaux, M. Michard, N. Grosjean, Combining PIV, POD and vortex identification algorithms for the study of unsteady turbulent swirling flows, Meas. Sci. Technol. 12 (9) (2001) 1422–1429, http://dx.doi.org/10.1088/0957-0233/12/9/307.

[45] S. Tamaro, R. Zamponi, D. Ragni, C. Teruna, C. Schram, Experimental investigation of turbulent coherent structures interacting with a porous airfoil, Exp. Fluids 62 (2021) 94, http://dx.doi.org/10.1007/s00348-021-03170-2.

[46] E.J.G. Arcondoulis, Y. Liu, D. Ragni, F. Avallone, A. Rubio-Carpio, N. Sedaghatizadeh, Y. Yang, Z. Li, Internal shear layer and vortex shedding development of a structured porous coated cylinder using tomographic particle image velocimetry, J. Fluid Mech. 967 (2023) A17, http://dx.doi.org/10.1017/jfm.2023.473.

[47] R. Zamponi, S. Moreau, C. Schram, Rapid distortion theory of turbulent flow around a porous cylinder, J. Fluid Mech. 915 (2021) A27, http://dx.doi.org/10.1017/jfm.2021.8.

[48] H.G. Davies, The radiated fields of multipole point sources near a solid spherical surface, J. Fluid Mech. 43 (3) (1970) 597–606, http://dx.doi.org/10.1017/S0022112070002604.

[49] R. Zamponi, S. Satcunanathan, S. Moreau, D. Ragni, M. Meinke, W. Schröder, C. Schram, On the role of turbulence distortion on leading-edge noise reduction by means of porosity, J. Sound Vib. 485 (2020) 115561, http://dx.doi.org/10.1016/j.jsv.2020.115561.

[50] C. Norberg, Fluctuating lift on a circular cylinder: Review and new measurements, J. Fluids Struct. 17 (1) (2003) 57–96, http://dx.doi.org/10.1016/S0889-9746(02)00099-3.

[51] R. Zamponi, S. Satcunanathan, S. Moreau, M. Meinke, W. Schröder, C. Schram, Effect of porosity on Curle's dipolar sources on an aerofoil in turbulent flow, J. Sound Vib. 542 (2023) 117353, http://dx.doi.org/10.1016/j.jsv.2022.117353.

[52] S.A.L. Glegg, W. Devenport, Aeroacoustics of Low Mach Number Flows: Fundamentals, Analysis, and Measurement, Academic Press, London, 2017.

[53] S. Li, D.E. Rival, X. Wu, Sound source and pseudo-sound in the near field of a circular cylinder in subsonic conditions, J. Fluid Mech. 919 (2021) A43, http://dx.doi.org/10.1017/jfm.2021.404.

[54] L.M. Milne-Thomson, Theoretical Hydrodynamics, Dover Publications, New York, 1996.

[55] J.E. Ffowcs Williams, D.L. Hawkings, Sound generation by turbulence and surfaces in arbitrary motion, Philos. Trans. Royal Soc. A 264 (1151) (1969) 321–342, http://dx.doi.org/10.1098/rsta.1969.0031.

[56] Z. Li, T. Tang, Y. Liu, E.J.G. Arcondoulis, Y. Yang, Numerical study of aerodynamic and aeroacoustic characteristics of flow over porous coated cylinders: Effects of porous properties, Aerosp. Sci. Technol. 105 (2020) 106042, http://dx.doi.org/10.1016/j.ast.2020.106042.

[57] J.M. Turner, J.W. Kim, Quadrupole noise generated from a low-speed aerofoil in near- and full-stall conditions, J. Fluid Mech. 936 (2022) A34, http://dx.doi.org/10.1017/jfm.2022.75.